Myosin 1b regulates intestinal epithelial morphogenesis via interaction with UNC45A

Céline Revenu, Corinne Lebreton, Magda Cannata Serio, Marion Rosello, Rémi Duclaux-Loras, Karine Duroure, Ophelie Nicolle, Fanny Eggeler, Marie-Thérèse Prospéri, Julie Stoufflet, et al.

Cell Reports

Myosin 1b regulates intestinal epithelial morphogenesis via interaction with UNC45A

Graphical abstract

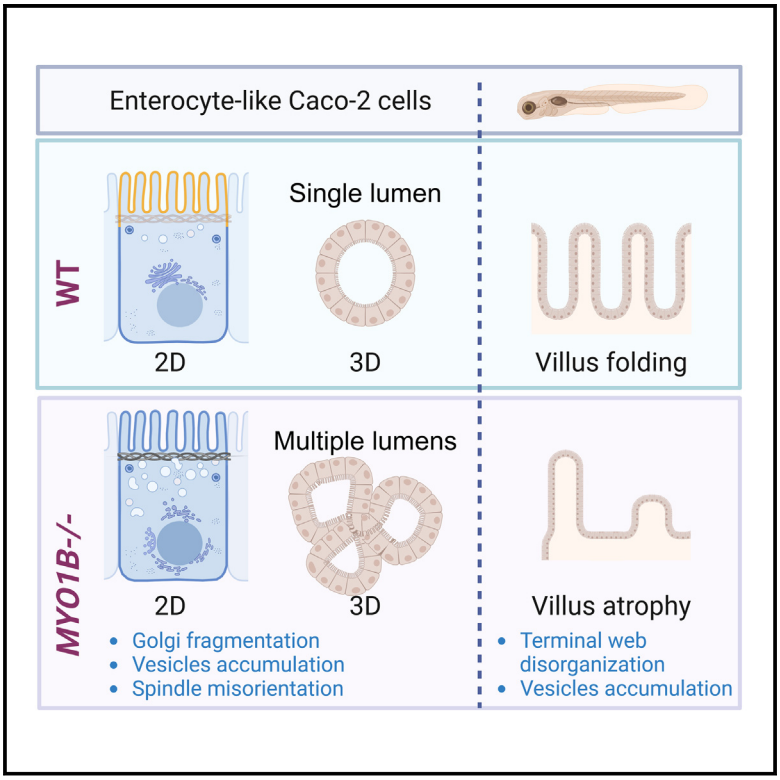

Highlights

- MYO1B is part of UNC45A interactome and is misfolded in UNC45A deficiency
- MYO1B contributes to lumenogenesis by modulating spindle orientation *in vitro*
- Loss of Myo1b causes villous-atrophy-like defects in the intestinal epithelium in zebrafish
- Loss of Myo1b causes terminal-web structural defects in the intestinal epithelium *in vivo*

Authors

Céline Revenu, Corinne Lebreton, Magda Cannata Serio, ..., Franck Perez, Marianna Parlato, Filippo Del Bene

Correspondence

marianna.parlato@inserm.fr (M.P.), filippo.del-bene@inserm.fr (F.D.B.)

In brief

Revenu et al. show the function of myosin 1b (Myo1b) in intestinal epithelia. In human cells, MYO1B is part of the UNC45A interactome and contributes to lumenogenesis by modulating spindle orientation *in vitro*. In zebrafish Myo1b is important for intestinal epithelium folding during the development of the intestinal bulb.

Revenu et al., 2024, Cell Reports *43*, 114941
December 24, 2024
https://doi.org/10.1016/j.celrep.2024.114941

CellPress

Cell Reports

CellPress
OPEN ACCESS

Report

Myosin 1b regulates intestinal epithelial morphogenesis via interaction with UNC45A

Céline Revenu,[1,2,6] Corinne Lebreton,[3,6] Magda Cannata Serio,[4,6] Marion Rosello,[1,2] Rémi Duclaux-Loras,[3] Karine Duroure,[1,2] Ophélie Nicolle,[5] Fanny Eggeler,[2] Marie-Thérèse Prospéri,[4] Julie Stoufflet,[1] Juliette Vougny,[1] Priscilla Lépine,[4] Grégoire Michaux,[5] Nadine Cerf-Bensussan,[3] Evelyne Coudrier,[4] Franck Perez,[4] Marianna Parlato,[3,7,*] and Filippo Del Bene[1,2,7,8,*]

[1]Institut Curie, PSL Research University, INSERM U934, CNRS UMR3215, 75248 Paris Cedex, France
[2]Sorbonne Université, INSERM, CNRS, Institut de la Vision, 75012 Paris, France
[3]INSERM, UMR1163, Laboratory of Intestinal Immunity and Institut Imagine, 75015 Paris, France
[4]Institut Curie, PSL Research University, Sorbonne Université, CNRS, UMR 144, Paris, France
[5]Université de Rennes, CNRS, IGDR (Institut de Génétique et de Développement de Rennes), UMR 6290, 35000 Rennes, France
[6]These authors contributed equally
[7]These authors contributed equally
[8]Lead contact
*Correspondence: marianna.parlato@inserm.fr (M.P.), filippo.del-bene@inserm.fr (F.D.B.)
https://doi.org/10.1016/j.celrep.2024.114941

SUMMARY

Vesicle trafficking and the establishment of apicobasal polarity are essential processes in epithelial morphogenesis. *UNC45A* deficiency has been reported in a multi-organ syndrome presenting with severe diarrhea associated with enterocyte polarity defects. Myosin 1b, an actin motor able to bind membranes, regulates membrane shaping and vesicle trafficking. Here, we show that MYO1B is part of the UNC45A interactome. In the absence of UNC45A, myosin 1b is degraded and forms aggregates when proteasome activity is inhibited. In 3D Caco-2 cells, lumen formation is impaired in the absence of myosin 1b, associated with spindle orientation defects, Golgi apparatus fragmentation, and trafficking impairment. In zebrafish larvae, loss of *myo1b* results in intestinal bulb epithelium folding defects associated with terminal web disorganization and vesicle accumulation, reminiscent of villous atrophy. In conclusion, we show that myosin 1b plays an unexpected role in the development of the intestinal epithelium downstream of UNC45A, establishing its contribution in the gut defects reported in UNC45A patients.

INTRODUCTION

The establishment of apicobasal polarity and lumen formation are two fundamental steps during vertebrate intestinal epithelial morphogenesis.[1] The actin cytoskeleton and vectorial vesicle trafficking play a major role in the initiation and maintenance of this process, leading to a stable single layer of cells with distinct apical and basolateral domains.[2,3] The apical membrane of the enterocyte is further organized into microvilli, plasma membrane protrusions supported by bundles of parallel actin filaments and interacting proteins interconnected at the basis through a network of actin, cytokeratins, spectrin, and myosins known as the terminal web (TW).[4,5] The interaction between neighboring polarized cells is strengthened by the formation of cadherin-based adherens junctions and claudin-based tight junctions.[5] This proper polarization of the intestinal epithelium is essential to achieving its main physiological roles, such as fluids and nutrient absorption and secretion. Accordingly, inherited epithelial cell polarity defects result in early-onset intestinal failure and diarrhea, usually appearing in the first days of life.[6,7] This is notably the case for microvillus inclusion disease (MVID), which is caused by loss-of-function (LOF) variants in *MYO5B*[8] and *UNC45A*, encoding type Vb myosin motor protein and its chaperone, respectively.[9–11] Lack of microvilli, appearance of microvillus inclusions, large intracellular vacuolar structures lined by microvilli, and accumulation of intracellular vesicles are typically observed in MYO5B- and UNC45A-deficient enterocytes.[9–11] Yet UNC45A promotes the folding of other myosins, and its role in intestinal epithelium may be more complex.[9]

Among these potential additional clients of Unc45A, myosins 1 are single-headed actin motors targeted to membranes. *In vitro* studies have demonstrated that myosin 1b (Myo1b) associates with organelles and regulates membrane trafficking by controlling their morphology.[12] Myo1b is also implicated in the formation of repulsive filopodia, which drive cell repulsion,[13] as well as in the formation of axons by regulating actin waves and the redistribution of actomyosin fibers in cultured neurons.[14] Further investigations have shown that Myo1b pulls out membrane tubes along actin bundles immobilized on a solid substrate,[15] acts as an actin depolymerase, and can flatten and prune branched actin filaments.[16,17] Despite these advances in understanding MYO1B function *in vitro* and in cellular systems, its

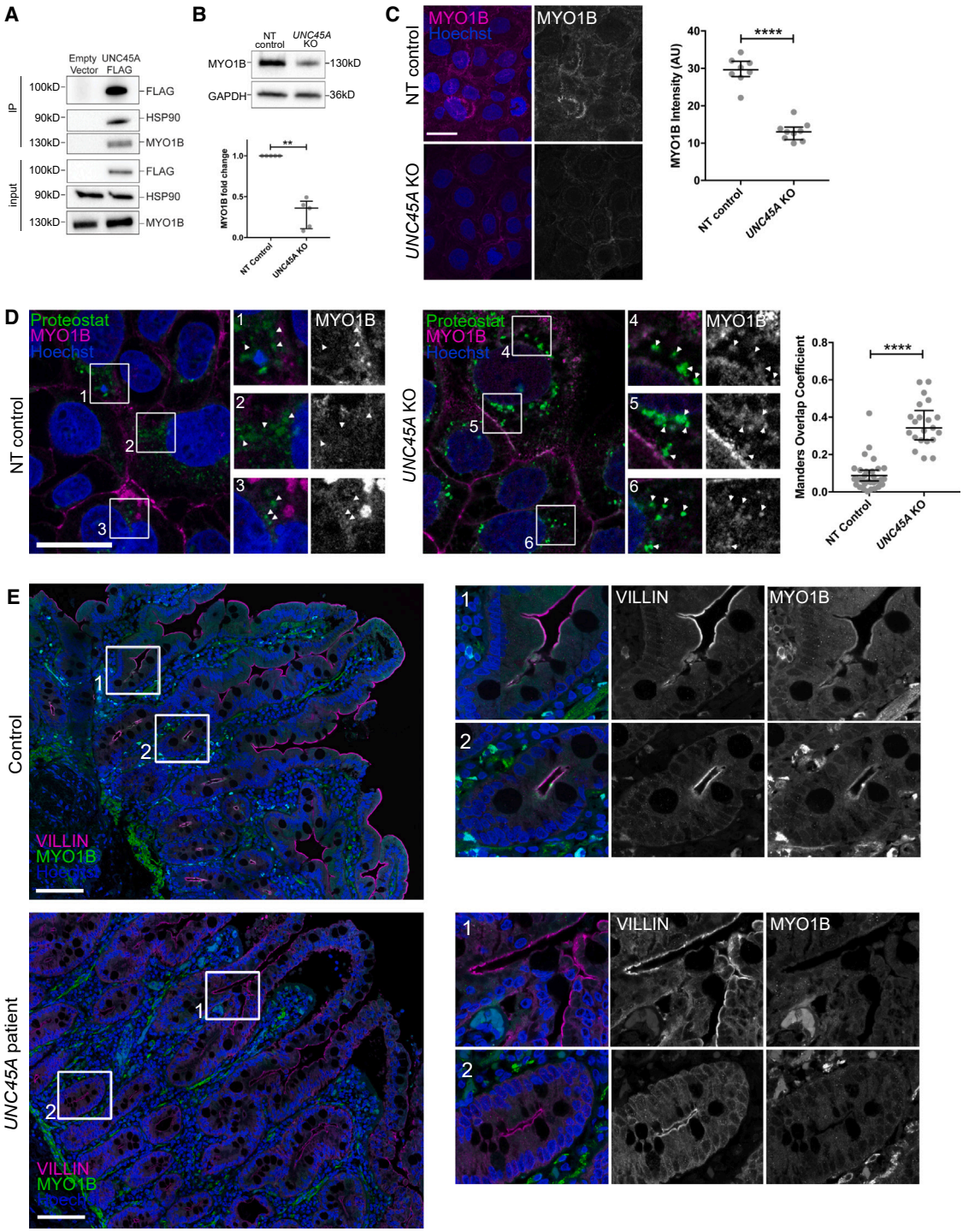

Figure 1. MYO1B interacts with UNC45A and is misfolded in UNC45A-depleted cells and in biopsies from UNC45A-deficient patient

(A) Coimmunoprecipitation of UNC45A with MYO1b and HSP90 in Caco-2 cells transduced with empty vector (EV) or FLAG/MYC-UNC45A.

(B) Western blot analysis of *UNC45A* Caco-2 KO cells and NT control lysates using anti-MYO1b antibody and relative quantification (n = 5).

(C) Immunohistochemistry analyses and quantification of MYO1b intensity in NT control (n = 8) and *UNC45A* KO (n = 9) Caco-2 cells. Pictures are maximal projections of confocal stacks; Hoechst labels nuclei. Scale bar, 30 μm.

(D) Confocal sections of NT control and *UNC45A* KO Caco-2 cells treated with the proteasome inhibitor MG132 and stained for MYO1b and with the aggresome probe Proteostat and quantification of the colocalization (NT n = 32; KO n = 21). Hoechst labels nuclei. Scale bar, 30 μm. Boxed areas shown in insets are enlarged 2×. Arrowheads point at Proteostat-labeled protein aggregates and highlight colocalization with MYO1B proteins in *UNC45A* KO cells.

(legend continued on next page)

function in tissue biology, especially in the intestinal epithelium where it is expressed, remains unexplored. Here, we investigate the interaction between MYO1B and UNC45A, as well as its role in the morphogenesis of the intestinal epithelium using human biopsies from healthy donors and UNC45A-deficient patients, Caco-2 cells, and *in vivo* zebrafish models.

We show that MYO1B is part of the UNC45A interactome and that its expression is strongly reduced in UNC45A-deficient patients and Caco-2 cells. The loss of MYO1B impairs epithelial morphogenesis in Caco-2 cells and *in vivo*, revealing its conserved function during normal intestinal epithelium development and morphogenesis.

RESULTS

Myosin 1b interacts with UNC45A and is misfolded in UNC45A deficiency

UNC45A acts in complex with HSP90 as a critical cochaperone for the folding and stability of type II myosins.[18] Immunoprecipitation coupled to mass spectrometry using UNC45A as bait in human epithelial colorectal Caco-2 cells has previously identified MYO1B as part of the UNC45A interactome in Caco-2 cells.[9] Lysates from Caco-2 cells overexpressing either myc/FLAG-tagged UNC45A or myc/FLAG-tagged empty vector (EV) were immunoprecipitated with myc-Ab, and pull-downs were analyzed by western blot, confirming the interaction of wild-type (WT) UNC45A with both MYO1B and HSP90 (Figure 1A). In addition, *UNC45A* KO Caco-2 cells showed reduced MYO1B expression by both western blot (Figure 1B) and immunofluorescence (Figure 1C), suggesting that in UNC45A-deficient condition MYO1B fails to fold properly and is redirected for proteasome degradation. Accordingly, blocking the proteasome machinery with the inhibitor MG132 induced the appearance of protein aggregates in *UNC45A* knockout (KO) Caco-2 cells (Figure 1D), where the MYO1B staining partly colocalized with the aggresomes (Figure 1D). Strikingly, while in control duodenal tissues, MYO1B was detected apically at the base of the villi and in crypts, partially colocalizing with VILLIN. In duodenal tissue from an UNC45A-deficient patient, VILLIN was still localized apically whereas MYO1B was barely detectable (Figure 1E). Overall, these findings confirm MYO1B as client of the chaperone complex UNC45A/HSP90 and indicate that MYO1B is misfolded, degraded, and therefore not functional in an UNC45A-deficient condition.

Myo1b is expressed apically in intestinal epithelial cells and contributes to lumenogenesis

To determine whether human MYO1B plays a conserved role in controlling intestinal epithelial cell morphogenesis, we used Caco-2 cells, which organize into polarized spherical cysts when cultured in three dimensions and therefore enable screening for morphogenesis defects. *MYO1B* accumulated apically in polarized Caco-2 cysts, as demonstrated by its localization in the actin-rich microvilli area and/or the subjacent TW (Figure S1A). *MYO1B* was then knocked out using CRISPR-Cas9 in Caco-2 cells (*MYO1B* KO, Figures S1A and S1B). After 5 days in Matrigel, *MYO1B* KO cells showed a significant increase of more than 75% of the percentage of cysts harboring multiple lumens compared to controls (Figures 2A–2C), suggesting a role for MYO1B in controlling lumen morphogenesis in intestinal epithelial cells, a phenotype previously reported for MYO5B.[19] The multi-lumen phenotype could be attributed to apical trafficking defects with subsequent alteration of the brush border. To investigate the dynamics of trafficking of cargoes, we employed the retention using selective hooks (RUSH) assay,[20] which allows synchronized release and tracking of cargo proteins from the endoplasmic reticulum (ER) to the Golgi and beyond (Figures 2D–2F). The trafficking of the two apical cargoes, a glycosylphosphatidylinositol anchored protein (GPI) and the intestinal alkaline phosphatase (ALPI), was assessed in Caco-2 *MYO1B* KO and *MYO5B* KO cells and compared to non-targeting (NT) control cells, all stably expressing these proteins. In *MYO1B* KO cells, both cargoes initially showed a slight delay in Golgi to plasma membrane (PM) trafficking, but ultimately exited the Golgi and reached the PM with almost normal kinetics. In contrast, ALPI and GPI trafficking was significantly impaired in *MYO5B* KO cells (Figures 2D, 2F, and S2; Videos S1, S2, S3, S4, S5, and S6). Defective early sorting from the Golgi apparatus and delivery to the PM could be due to a globally impaired Golgi function. Thus, detailed localization analysis of two Golgi markers, giantin (a marker of the *cis*- and medial-Golgi[21]) and golgin-97 (a marker of the *trans*-Golgi network[22]) revealed Golgi fragmentation in *MYO5B* KO cells, consistent with previous observations.[23] Interestingly, our findings extended these observations to *MYO1B* KO cells, where mild but significant Golgi fragmentation was observed when compared to WT cells (Figures 2G and 2H). Overall, our findings show that while MYO1B is involved in early trafficking stages, its loss does not affect the final delivery of apical targets to the membrane. Accordingly, the global apical polarity of Caco-2 cysts was not affected in *MYO1B* KO cells compared to controls as shown by the correct apical concentration of F-actin, pERM, and Villin (Figures 2A and 2B). In line with this finding, stimulated emission depletion (STED) super-resolution microscopy did not show a major difference in phalloidin-labeled microvilli density between control and *MYO1B* KO Caco-2 cells, whereas it was strongly reduced in the *MYO5B*-deficient condition (Figure S1C).

Loss of MYO1B causes misorientation of the mitotic spindle

To assess whether endocytic trafficking was impaired, we looked at the distribution of the lysosomal marker LAMP1 in both *MYO1B*- and *MYO5B*-deficient Caco-2 cells. A significant accumulation of large cytoplasmic vacuole-like intracellular structures that were positive for LAMP1 was found clustering at the perinuclear region of the cell in both *MYO1B* KO and

(E) Confocal sections of a human biopsy from a control and from a UNC45A LOF patient immunolabeled for the microvilli marker Villin and for MYO1b; Hoechst labels nuclei. Scale bar, 100 μm. Boxed areas shown in insets are enlarged 3× and highlight the apical localization of MYO1b in duodenal control tissue at the base of the villi (1) and in crypts (2).

Data presented in (B), (C), and (D) are shown as median and interquartile range; Mann-Whitney test $^{**}p < 0.01$, $^{****}p < 0.0001$.

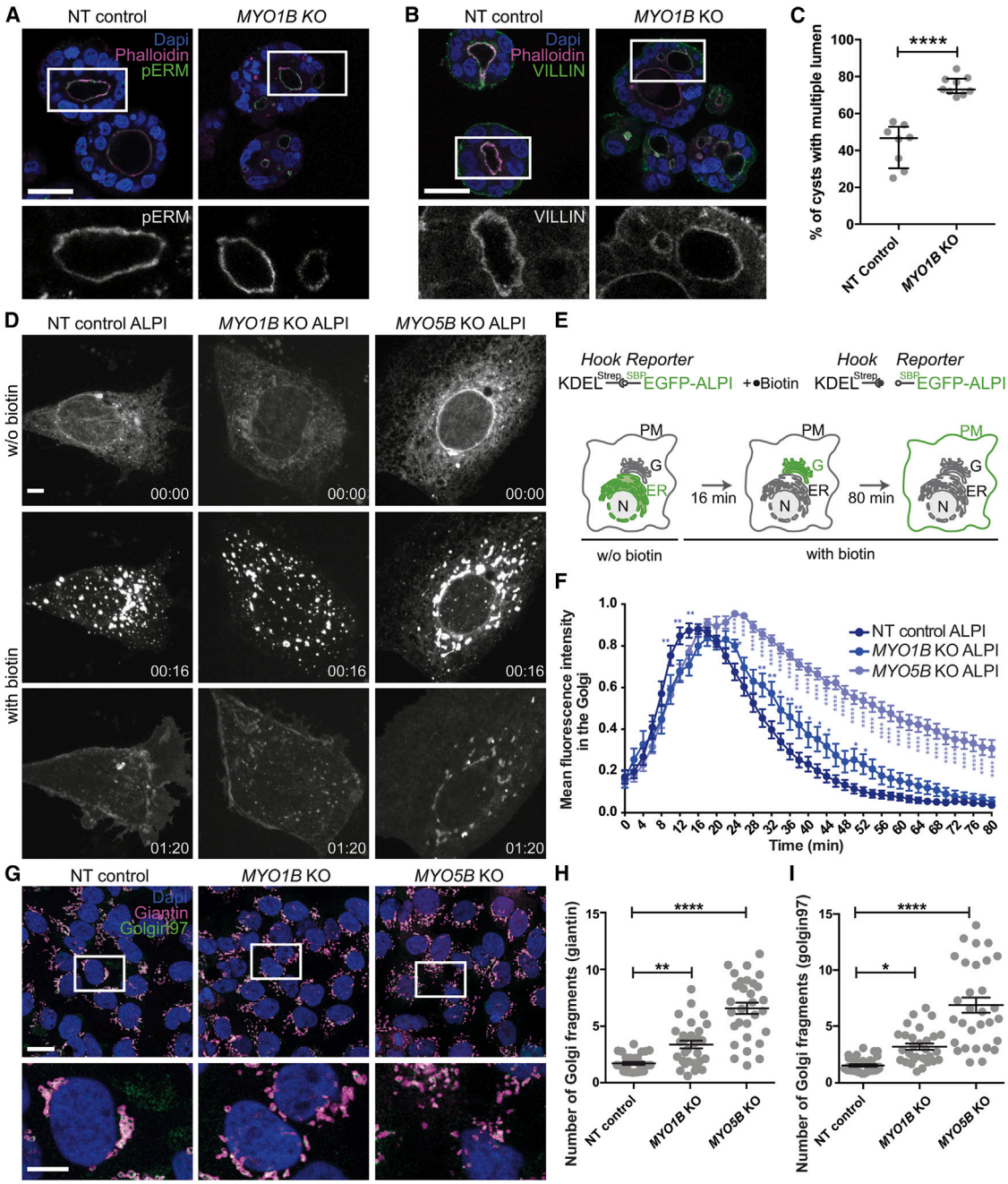

Figure 2. MYO1B loss impairs enterocyte 3D organization and trafficking despite normal apicobasal polarization

(A and B) Confocal sections of NT control and *MYO1B* KO Caco-2 3D cultures stained for the apical and microvilli markers phospho-Ezrin (pERM, A) and Villin (B). F-actin (phalloidin) and nuclei (DAPI) are stained. Scale bars, 30 μm. Boxed areas shown in insets are enlarged 2.5×.

(C) Quantification of the percentage of well-formed cysts with a single central lumen in NT control and MYO1B KO Caco-2 3D cultures. In total, 115 cysts from eight fields (NT) and 379 cysts from nine fields (KO) were analyzed. Data are presented as median and interquartile range; Mann-Whitney $^{****}p < 0.0001$.

(D) Imaging of the synchronized transport of stably expressed SBP-EGFP-ALPI (intestinal alkaline phosphatase) in Caco-2 NT, *MYO1B* KO, and *MYO5B* KO cells. Streptavidin-KDEL was used as an ER hook. Release from the ER was induced by addition of biotin at 0 min. Scale bar, 50 μm.

(E) Schematics of the RUSH assay. PM, plasma membrane; ER, endoplasmic reticulum; G, Golgi; N, nucleus.

(F) Kinetics of arrival of ALPI in Caco-2 NT, *MYO1B* KO, and *MYO5B* KO (color) cells to the cell surface after release from the ER. See also Videos S1, S2, and S3. Caco-2 NT $n = 30$, *MYO1B* KO $n = 26$, *MYO5B* KO $n = 22$, two-way ANOVA followed by a Bonferroni multiple comparison test. ns, not significant; $^{*}p < 0.5$, $^{***}p < 0.001$, $^{****}p < 0.0001$.

(legend continued on next page)

MYO5B KO cells (Figure 3A). In MYO5B-deficient conditions, these vesicles are thought to impair the orientation of the mitotic spindle.[24] As mispositioning of the newly generated apical surface after cell division could also account for the multi-lumen phenotype observed in MYO1B-deficient conditions, we assessed the orientation of the mitotic spindle. Cells were cultured in coverslips, and microtubules were labeled with β-tubulin and DNA with Hoechst 33342 to visualize the mitotic spindle. The orientation of the mitotic spindle relative to the substratum (x-z direction) in cell monolayers was determined in 3D-reconstructed confocal images (x-y direction) of fixed cells by measuring the angle (β) between a line drawn through the spindle poles and a line parallel to the substratum (Figure 3B). During metaphase, while the mitotic spindle of WT cells was almost parallel to the substratum, *MYO1B* KO cells displayed increased oscillations of the mitotic spindle angle, similar to what was observed in *MYO5B* KO cells (Figure 3B).

Myo1b concentrates apically in the gut epithelium but is not involved in epithelial cell differentiation of zebrafish intestinal bulb

To investigate the role of Myo1b in intestinal epithelium morphogenesis *in vivo*, we used zebrafish as a model organism. The zebrafish intestinal epithelium differentiates from 3 days post fertilization (dpf), when it is essentially a flat monolayered tube. At 5 dpf, epithelial folds are present, especially in the anteriormost part of the gut, the intestinal bulb.[25] These folds are equivalent to the mammalian villi, and although no crypts are present in zebrafish, the regions between folds have a crypt-like role.[26] There is one single *myo1b* gene with several splicing isoforms in the current zebrafish genome assembly. The corresponding Myo1b protein shares 80% identity with the *Homo sapiens* and *Mus musculus* homologs (Figure 4A). To determine the expression pattern of *myo1b* during zebrafish development, we performed whole-mount *in situ* hybridization labeling with specific antisense probes. *Myo1b* transcripts were unambiguously detected at 3 dpf in the digestive tract of zebrafish, which corresponds to the onset of gut morphogenesis,[25,27] and at 5 dpf (Figure 4B), when the intestine becomes functional and compartmentalized in bulb, mid, and posterior intestines. At this stage, the transcripts were restricted to the intestinal bulb, the anterior part of the gut that forms large folds. To assess the subcellular localization of Myo1B protein and owing to the lack of a suitable antibody, we expressed in the gut an eGFP-tagged Myo1b construct that revealed apical accumulation of the protein (Figure 4C). The potential role of Myo1b in the morphogenesis of the intestinal epithelium was investigated via LOF experiments. First, we designed a splice-blocking Morpholino (Myo1b-MO) that efficiently prevents proper splicing of *myo1b* as determined by RT-PCR (Figures S3A and S3B). At the concentration used, Myo1b-MO displayed no overt phenotype, despite occasionally a slight heart edema (Figure S3C). To extend these results, we also generated a mutated allele at the *myo1b* locus using the CRISPR-Cas9 system, resulting in the insertion of a single base at the beginning of the open reading frame, as confirmed by sequencing (Figure S3D). This leads to a premature stop codon and to the lack of detection of the protein by western blot in gut lysates from adult homozygote mutants (*myo1b*$^{-/-}$, Figure S3E). As *myo1b* mRNA is maternally provided (Figure S3F), the maternal contribution was suppressed by crossing *myo1b*$^{-/-}$ females. As for the MO injections, the resulting maternal-zygotic homozygous mutant larvae displayed no overt phenotype (Figure S3C). In cross-sections (Figure 4D), the intestinal bulbs of Myo1b-MO and *myo1b*$^{-/-}$ larvae appeared smaller compared to controls. A significant reduction of the number of cells per cross-section was observed for both Myo1b-MO and *myo1b*$^{-/-}$ intestinal bulbs at 3 and 5 dpf compared to their respective controls (Figure 4E). A reduction in the total cell number in the intestinal bulb could be the consequence of increased apoptosis or reduced cell proliferation. No significant difference with controls in the proportion of proliferative cells could be detected at 3 and 5 dpf (Figure S4A). A slight increase in the proportion of apoptotic cells could be detected at 5 dpf but not at 3 dpf (Figure S4B). This later increase in apoptosis, however, cannot account for the reduced cell number per section reported from 3 dpf on and could more likely be a readout of increased cellular stress level upon prolonged absence of Myo1b, as reported after the KO of other myosins 1 in mouse and *Drosophila*.[28,29] Using specific markers for secreting and absorptive cell lineages, defects in enterocyte differentiation could also be excluded (Figures S4C and S4D). In *myo1b*-depleted mutants, phalloidin staining did not reveal microvillus inclusions, ultrastructures lined internally by microvilli which represent the hallmark feature of MVID (Figure 4F), in contrast to what has been previously observed in *myo5b* zebrafish mutant.[30] In addition, the microvilli marker Villin appeared properly localized apically, lining the lumen together with F-actin (Figure 4F), overall suggesting that global apical polarity is not affected in Myo1b MO and *myo1b* $^{-/-}$ intestinal epithelium *in vivo*, in keeping with results obtained in *MYO1B*-deficient Caco-2 cells.

Loss of Myo1b causes villus-atrophy-like features in the intestinal bulb epithelium in zebrafish

To analyze 3D intestinal bulb epithelium morphogenesis in zebrafish, we used the BAC line *cldn15la*:cldn15la-GFP that specifically labels the gut epithelium.[31] Both MO and KO intestinal bulbs revealed single continuous lumen, suggesting that early steps of lumen fusion events were not affected.[31,32] However, in Myo1b-MO larvae, the intestinal bulb epithelium appeared mostly flat at 5 dpf, not developing the expected folds observed

(G) Confocal sections of NT control, *MYO1B* KO, and *MYO5B* KO Caco-2 cells stained for the *cis*- and medial-Golgi marker giantin, the *trans*-Golgi network marker golgin97, the *cis*- and medial-Golgi marker giantin, and nuclei (DAPI). Scale bar, 20 μm. Insets are provided as white boxes for better visualization (scale bar, 10 μm).

(H and I) Quantification of the Golgi fragmentation was determined using deconvolved images to sharpen the distinction between Golgi apparatus and general cytosplasmic fluorescence. Deconvolved images were then segmented based on the intensity of the giantin fluorescence (H) and golgin97 (I), and the number of Golgi fragments was determined using Imaris software. Thirty cells were analyzed for each data point. Data are shown as median ± SEM. Caco-2 NT $n = 30$, *MYO1B* KO $n = 30$, *MYO5B* KO $n = 30$; ordinary one-way ANOVA followed by a Bonferroni multiple comparisons test. $^{*}p < 0.05$, $^{**}p < 0.01$, $^{****}p < 0.0001$.

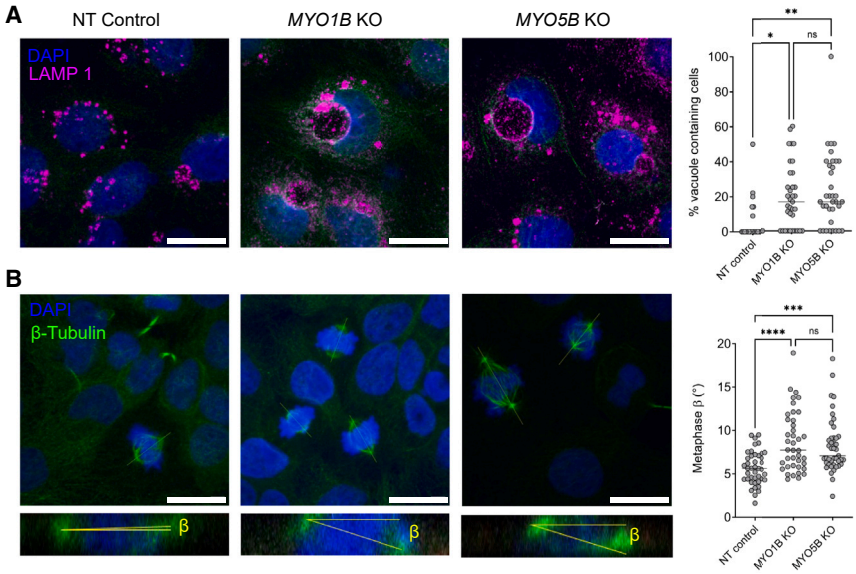

Figure 3. MYO1B loss impairs membrane recycling and spindle orientation

(A) Confocal sections of NT control, *MYO1B* KO, and *MYO5B* KO Caco-2 3D cultures stained for the lysosome marker LAMP1 and DAPI, and quantification of the percentage of vacuoles containing cells (Caco-2 NT $n = 22$, *MYO1B* KO $n = 35$, *MYO5B* KO $n = 35$). Scale bars, 20 μm.

(B) Confocal sections of NT control and *MYO1B* KO Caco-2 3D cultures stained for β-tubulin and DAPI. The β angle between the spindle axis and the substratum in the confocal x-z dimension was quantified in metaphase (Caco-2 NT $n = 42$, *MYO1B* KO $n = 40$, *MYO5B* KO $n = 44$). Scale bars, 20 μm.

Data are presented as median; one-way ANOVA test, $^{*}p < 0.05$, $^{**}p < 0.01$, $^{***}p < 0.001$, $^{****}p < 0.0001$.

in controls (Figure 5A). Consistently with this phenotype, in the KO model we detected a significant reduction in fold length in KO versus control samples (Figure 5B). In an attempt to understand this milder phenotype in the mutant compared to the MO condition, we assessed potential compensation mechanisms by other myosins 1 by performing RT-qPCR. On the four myosins 1 tested (*myo1ca*, *myo1cb*, *myo1d*, and *myo1eb*), *myo1eb* showed a reproducible increase of on average 60% of the WT expression level in the mutant using *ef1a* (Figure S3G) as reference gene. *Myo1eb* is broadly expressed in early developmental stages but has restricted expression patterns after 2 dpf (mostly branchial arches and pharynx).[33] A partial compensation of the loss of *myo1b* by an upregulation of *myo1eb* could thus potentially explain the subtler and more restricted phenotype of the mutant larvae compared to the knockdowns (Figure S3F).

Loss of Myo1b causes accumulation of vesicles and terminal-web structural defects

To further characterize the architecture of intestinal bulb epithelium, an ultrastructural analysis by transmission electron microscopy (TEM) was performed on 5-dpf larvae. This confirmed the affected folding of the intestinal bulb epithelium in MO and KO samples and the preserved global apicobasal polarity of enterocytes (Figures 5C and 5D). Quantifying microvilli length and density did not reveal any significant defect resulting from Myo1b depletion, although packing looked less regular (Figure 5E). However, Myo1b depletion induced accumulation of electron-lucent vesicles in the enterocyte cytoplasm of MO and KO samples compared to controls (Figures 5D [insets] and 5F), overall suggesting defects in apical endocytosis. Moreover, TEM showed that the TW, the apical cytoskeleton composed of actin and intermediate filaments, appeared as electron-dense material in Myo1b-MO and *myo1b*$^{-/-}$ mutant larvae (Figures 5D and 5E). Quantifications confirmed a higher-electron-intensity subapical/cytoplasmic ratio in the morphants and mutants compared to WT (Figure 5G). We thus visualized the localization of TW intermediate filaments using a pan-cytokeratin antibody. Contrary to its apical localization in WT larvae, cytokeratin mislocalized to lateral and cytoplasmic regions of the enterocytes, confirming the perturbation of the TW organization in *myo1b*-depleted larvae (Figure 5H). These phenotypes, including reduced epithelium folding and altered apical pole ultrastructure observed in the zebrafish mutants, indicate that Myo1b plays a conserved role in gut epithelium morphogenesis.

DISCUSSION

Establishment of apical-basal polarity of epithelial cells is critical to maintaining gut morphogenesis and assuring the absorptive function of the intestine. Defective brush border structure and reductions in microvillar density result in malabsorption and diarrhea, common features of a group of inherited defects caused by variants in genes coding for critical effectors of intestinal epithelial function.[6] Among those, severe intestinal disorders caused by LOF variants in genes including *MYO5B* and its cochaperone *UNC45A* feature alterations in apical trafficking and recycling, resulting in functional disorganization of the brush border with sparse microvilli and mislocalization of apical proteins, lysosome accumulation, and microvillus inclusions.[7,9] Yet UNC45A participates in the functional maturation of other myosins. Our results in UNC45A-deficient enterocyte-like Caco-2 cells and in UNC45A-deficient patient tissues indicate a strong reduction in the protein level of MYO1B, pointing to its destabilization in the absence of a functional UNC45A and suggesting that the intestinal phenotypes associated with LOF variants in UNC45A could, hence, partly be the consequence of loss of MYO1B.

Knocking out *MYO1B* in Caco-2 cells affects central lumen formation without perturbing global apical polarity and brush border assembly, a result in contrast with what is observed in the MYO5B-deficient condition, where a defect in central lumen formation is associated with a severe defect in apical protein targeting resulting in lack of microvilli in Caco-2 cells. Both MYO1B and MYO5B deficiencies are characterized by early trafficking defects, which are associated with increased Golgi fragmentation and the

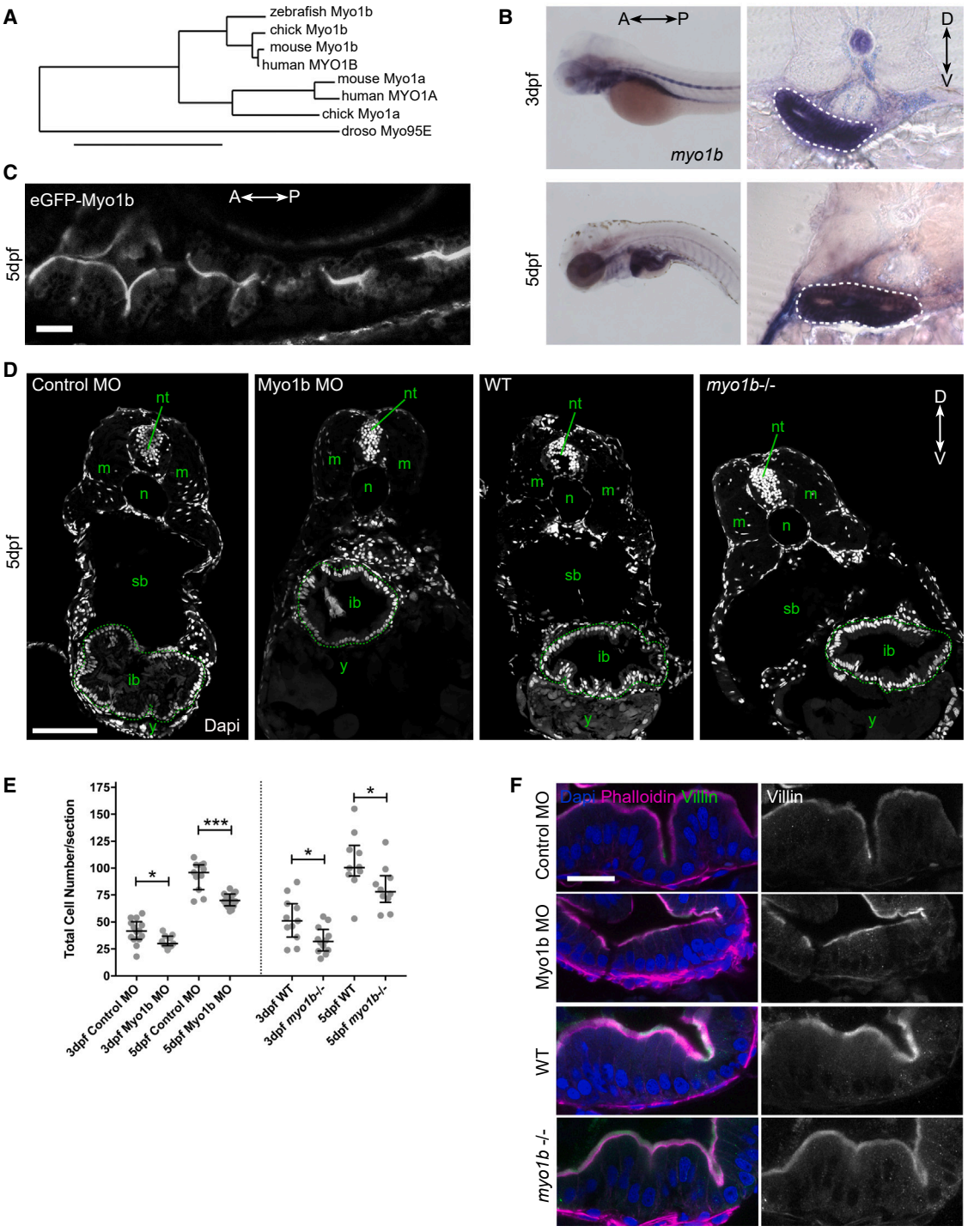

Figure 4. Myo1b localizes apically in the zebrafish gut epithelium but is not involved in epithelial cell differentiation

(A) Phylogenetic tree based on protein sequence of zebrafish, chick, human, and mouse Myo1b and Myo1a and *Drosophila* Myo95E.

(B) *In situ* hybridization for *myo1b* transcripts on 3- and 5-dpf zebrafish larvae whole mounts (left panels) and cross-sections at the level of the intestinal bulb (right panels). On sections, the forming intestinal bulb is circled with white dashed lines.

(C) Live, longitudinal (anteroposterior axis) confocal section of the intestinal bulb of a 5-dpf zebrafish larva expressing the transcription activator KalT4 driving the expression of the eGFP-Myo1b transgene under the control of an upstream activating sequence in the gut epithelium. Scale bar, 30 μm.

(D) Confocal imaging of zebrafish section sections stained with DAPI of 5-dpf larvae injected with control and Myo1b MO, and 5-dpf WT and *myo1b*$^{-/-}$ larvae. ib, intestinal bulb (circled with dashed lines); m, muscles; n, notochord; nt, neural tube; sb, swim bladder; y, yolk. Scale bar, 100 μm.

(legend continued on next page)

formation of giant endosomes, features previously reported in the context of MYO5B deficiency.[24] Interestingly, it has been proposed that in MYO5B-depleted cells, the presence of oversized late endosomes within the cytoplasm of mitotic epithelial cells can disrupt the orientation of the mitotic spindle apparatus. This disruption can cause the mitotic spindle to misalign with the substratum, leading to aberrant cell-division orientation and disorganization of the epithelial monolayer. This physical hindrance of spindle alignment by abnormally large endosomes has been suggested as a key mechanism in this process.[24] Our findings demonstrate that in the absence of MYO1B, a similar mechanism results in comparable epithelial defects, specifically the formation of multi-lumen cysts. Notably, this occurs without any defects in the localization of apical markers, suggesting that the defects observed following MYO5B loss can be functionally uncoupled. This indicates that while MYO1B and MYO5B both influence lumen formation and endosome size, their function in apical protein trafficking and epithelial polarity maintenance can be distinctly separated as well as their contribution to MVID following UNC45A loss in humans.

In zebrafish, we report defects in epithelial folding and villous atrophy when Myo1b is depleted, overlapping the phenotype reported in *unc45a* zebrafish.[9,11] For this study, we analyzed both *myo1b* mutant- and MO-induced phenotypes. It is now well established that MO knockdowns often result in more severe overt phenotypes than the corresponding KOs, at least partially due to the induction of genetic compensation mechanisms in the mutants.[34,35] In the *myo1b* null case, we observed a more subtle outcome than with the MO, which could be due to compensation mechanisms[36] as supported by the RT-qPCR of *myo1eb*. Here, the intestinal bulb phenotypes observed with both approaches converged on a reduced cell number in intestinal bulb sections and impaired epithelial folding.

Up to now, Myo1a, Myo1c, Myo1d, and Myo1e have been identified in intestinal brush borders constituting the apical pole of differentiated enterocytes[37] and have been implicated in the maintenance of the intestinal epithelial differentiated state. Myo1a, which is associated with the highly organized actin network of differentiated enterocytes in mammals[29,38] but seems to lack these in the zebrafish and *Drosophila* genomes, is important for enterocyte polarity and participates in the structure and composition of the brush border.[29,39] The phenotype of the *myo1a* KO mice is, however, mild, with reports of clear compensations by other class I myosins.[29,37] Likewise, two of the known class I myosins in *Drosophila* are also localized in the apical pole of differentiated enterocytes, and *Drosophila* Myo61F is necessary for the stability of enterocyte apical organization.[28] Here we report the expression of another myosin 1 in the gut epithelium, Myo1b, and its apical localization in Caco-2 cells, enterocytes of duodenal human tissues, and enterocytes of zebrafish intestinal bulb. Myo1b localization in microvilli had previously been reported in kidney epithelial cells.[40] In human duodenum, Myo1b is expressed at the base of the villi and in crypts, suggesting a specific role in the proliferative compartment and not in the enterocyte differentiated state. We did not detect global polarization defects at the cell level or impaired differentiation in the absence of Myo1b, whereas both the Caco-2 3D model and the zebrafish model demonstrate morphogenetic defects at the tissue level, respectively single-lumen formation and folding.

Proliferation, apoptosis, or differentiation defects do not account for the reduced cell number observed on transverse sections of the intestinal bulb from 3 dpf. As the sections give a 2D overview of a 3D organ, this reduced cell number is thus likely the readout of the different organization in the space of the epithelium. A specificity of the zebrafish intestinal bulb is the early folding of the epithelium that remains pronounced to adulthood.[27] The reduced folding and villi formation in the mutants and morphants are clear signs of a different architecture of the tissue. Also, the mechanisms underlying intestinal epithelium folding are not yet fully understood. The impact of tension and forces at the cell and tissue level driving compression, cell intercalation, and invagination through apical constriction have been investigated in other tissues during development.[41] Myosins are central in the control of actin cytoskeleton dynamics and in force generation.[42] In particular, Myo1b deforms membranes and participates in organelle formation and trafficking.[12,43] It also remodels the actin cytoskeleton.[13,14,17] Its roles in membrane traffic and in the dynamic organization of actin structures make it a plausible actor in the morphogenesis of the gut epithelium. Electron microscopy data show a strong accumulation of intracellular vesicles in Myo1b mutant and MO tissues, suggesting impaired trafficking, in agreement with its role in the formation of post-Golgi carriers and protein transport at the level of multivesicular endosomes.[12,44] Electron microscopy and cytokeratin immunostaining also reveal modifications of the TW area, the apical actin belt linking adherens junctions in the epithelium, in agreement with its role in actin dynamics. Myo1b function in actin dynamics and, consequently, on membrane remodeling and membrane trafficking must impact cell and tissue mechanics,[45] and in this way contributes to impaired intestinal epithelial folding in the absence or downregulation of *myo1b*. MYO1B-restricted localization at the base of the villi in human biopsies may indicate a specific mechanical role in crypt morphogenesis. In conclusion, our work identifies a role for Myo1b in gut morphogenesis and implicates it as a potential player in the complex intestinal phenotype of UNC45A deficiency.

Limitations of the study

The conclusions drawn from this study primarily rely on data obtained from the human Caco-2 enterocyte-like line.

The Caco-2 line has limitations in fully representing the complexity of the enterocyte differentiation and polarization process. Though not used in this study, intestinal organoid cultures would likely provide a more accurate representation of these mechanisms and could offer more biologically relevant insights in future investigations.

(E) Quantifications from DAPI-stained sections of the total number of cells per section at 3 and 5 dpf in the four conditions. Data are presented as median and interquartile range; Mann-Whitney test, $*p < 0.05$, $***p < 0.001$.

(F) Imaging of zebrafish larval sections of the intestinal bulb at 5 dpf in the four conditions stained for the microvilli marker Villin, F-actin (phalloidin), and DAPI. Scale bar, 20 μm.

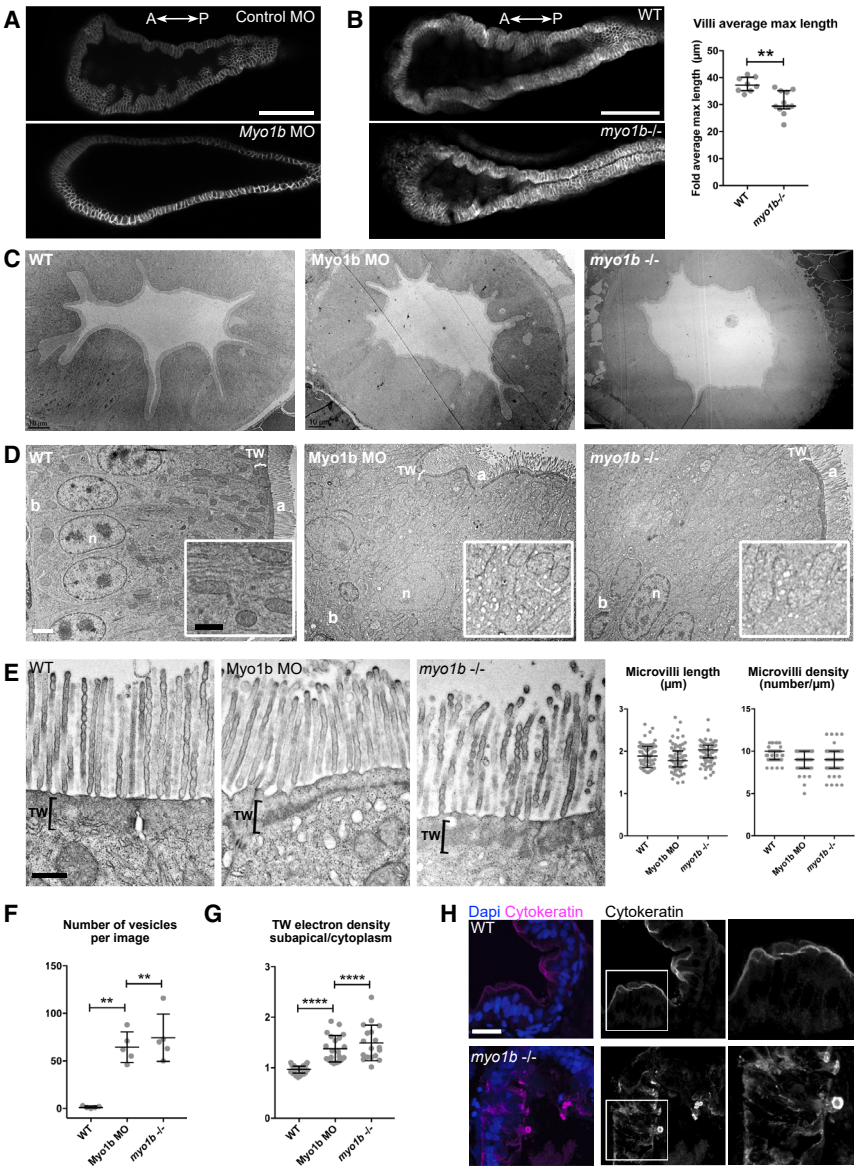

Figure 5. Loss of Myo1b causes villus atrophy-like features in the intestinal bulb epithelium in zebrafish

(A) Single confocal plane of live 5-dpf larvae expressing Cldn15la-GFP injected with control MO (top) and Myo1b-MO (bottom). Note the flat epithelium in the Myo1b MO condition. Scale bar, 100 μm.

(B) (Left) Single confocal planes of live 5-dpf WT (top) and *myo1b*$^{-/-}$ (bottom) larvae expressing Cldn15la-GFP. Scale bar, 100 μm. (Right) Quantification of the average length of the three longest folds per intestinal bulb analyzed. Data are presented as median and interquartile range (WT $n = 8$, *myo1b*−/− $n = 11$); Mann-Whitney test, $^{**}p < 0.01$.

(C and D) Transmission electron micrographs of sections of intestinal bulbs from WT, Myo1b MO, and *myo1b*$^{-/-}$ 5-dpf larvae presenting a general view of the folds of the epithelium (C; scale bar, 10 μm) and of the apicobasally polarized enterocytes (D; b, basal; a, apical; n, nuclei; scale bar, 2 μm). Insets in (D) show higher magnifications of the cytoplasm region (scale bar, 1 μm).

(E) Transmission electron micrographs of sections of intestinal bulbs from WT, Myo1b MO, and *myo1b*$^{-/-}$ 5dpf larvae illustrating the organization of the brush border. Scale bar, 500 nm. Quantifications of the average length and density of the intestinal microvilli in the different conditions ($n = 75$). Data presented are median and interquartile range.

(F and G) Quantification of vesicles ($n = 5$) (F) and TW electron density subapical/cytoplasm (G; WT $n = 27$, MO $n = 21$, *myo1b*$^{-/-}$ $n = 18$). Data are presented as median and interquartile range; Mann-Whitney test, $^{**}p < 0.01$, $^{****}p < 0.0001$.

(H) Imaging of sections of the intestinal bulb of WT and *myo1b*$^{-/-}$ 5-dpf larvae stained for the intermediate filament marker cytokeratin and DAPI. Scale bar, 20 μm.

RESOURCE AVAILABILITY

Lead contact

Requests for further information and resources should be directed to and will be fulfilled by the lead contact, Filippo Del Bene (filippo.del-bene@inserm.fr).

Materials availability

All unique/stable reagents generated in this study are available from the lead contact with a completed materials transfer agreement.

Data and code availability

- All data reported in the paper are available from the lead contact upon request.
- This paper does not report original code.
- Any additional information required to reanalyze the data reported in this paper is available from the lead contact upon request.

ACKNOWLEDGMENTS

The authors thank the Del Bene team for fruitful suggestions and discussions, the members of the Institut Curie zebrafish facility, and the pathologist Dr. Marion Rabant from Necker Hospital for providing intestinal tissues from UNC45A-deficient patients. We thank Nicolas Goudin from the Necker bioimaging analysis center for helping with the imaging analysis. The authors acknowledge the Cell and Tissue Imaging Platform (PICT-IBiSA, Institut Curie, Paris), the Cell and Tissue Imaging Platform of the Genetics and Developmental Biology Department (UMR3215/U934, Institut Curie, Paris), the MRic facility (Rennes), and all members of the French National Research Infrastructure France-BioImaging (ANR10-INBS-04) for help with light microscopy and electron microscopy. C.R. was supported by an EU H2020 Marie Skłodowska-Curie Action fellowship (H2020-MSCA-IF-2014 #661527). M.R. was supported by the Fondation pour la Recherche Médicale (FRM grant number ECO20170637481). The work in F.P.'s lab has been supported by the Fondation pour la Recherche Médicale (EQU201903007925), by the Agence

Nationale de la Recherche (ANR-19-CE13-0006-03, ANR-20-CE14-0017-02, ANR-19-CE13-0002-03, and ANR-11-LABX-0038), and has also received support under the program "Investissements d'Avenir" launched by the French Government and implemented by ANR with the references CelTisPhyBio (11-LBX-0038) and ANR-10-IDEX-0001-02 PSL. This work has been supported by Agence Nationale de la Recherche (ANR-20-CE17-0020 to N.C.-B., G.M., and F.D.B.)

AUTHOR CONTRIBUTIONS

C.R., N.C.-B., M.P., and F.D.B. conceived the project. J.S. and C.R. generated the Myo1b null allele in zebrafish. M.-T.P. generated the KO cells. M.R. generated the stable zebrafish transgenic lines. C.R., C.L., and F.E. performed immunofluorescence staining. K.D., J.V., and M.R. performed *in situ* hybridization. R.D.-L. performed western blotting and pull-down assay. K.D. and C.R. conducted the RT-qPCR analysis. J.S. and J.V. genotyped the mutants. O.N. performed TEM under the supervision of G.M. P.L. generated preliminary data with Morpholinos under the supervision of E.C. M.C.S. performed the RUSH assay under the supervision of F.P. C.R., M.P., and F.D.B. wrote the paper with input from all other authors. F.D.B. and M.P. supervised the work.

DECLARATION OF INTERESTS

The authors declare no competing interests.

STAR★METHODS

Detailed methods are provided in the online version of this paper and include the following:

- KEY RESOURCES TABLE
- EXPERIMENTAL MODEL AND STUDY PARTICIPANT DETAILS
  - Zebrafish (*Danio rerio*) husbandry
  - Experimental animal study approval
- METHOD DETAILS
  - CRISPR/Cas9 genome editing of *MYO1B* and *MYO5B* in Caco-2 cells
  - Real-time imaging of the synchronized secretion
  - Western blotting and pull down assay
  - Phylogenetic analysis
  - Molecular cloning
  - Zebrafish (*Danio rerio*) husbandry
  - *In situ* hybridization
  - Myo1b zebrafish mutant generation with CRISPR/Cas9
  - Morpholino oligonucleotide design and injections
  - Quantitative RT-PCR
  - Imaging
  - TEM analysis on zebrafish larvae
- QUANTIFICATION AND STATISTICAL ANALYSIS

SUPPLEMENTAL INFORMATION

Supplemental information can be found online at https://doi.org/10.1016/j.celrep.2024.114941.

Received: March 20, 2023
Revised: August 2, 2023
Accepted: October 17, 2024
Published: December 4, 2024

REFERENCES

1. Chin, A.M., Hill, D.R., Aurora, M., and Spence, J.R. (2017). Morphogenesis and maturation of the embryonic and postnatal intestine. Semin. Cell Dev. Biol. *66*, 81–93. https://doi.org/10.1016/j.semcdb.2017.01.011.
2. Lubarsky, B., and Krasnow, M.A. (2003). Tube morphogenesis: making and shaping biological tubes. Cell *112*, 19–28. https://doi.org/10.1016/s0092-8674(02)01283-7.
3. Martin-Belmonte, F., and Mostov, K. (2008). Regulation of cell polarity during epithelial morphogenesis. Curr. Opin. Cell Biol. *20*, 227–234. https://doi.org/10.1016/j.ceb.2008.01.001.
4. Revenu, C., Athman, R., Robine, S., and Louvard, D. (2004). The co-workers of actin filaments: from cell structures to signals. Nat. Rev. Mol. Cell Biol. *5*, 635–646. https://doi.org/10.1038/nrm1437.
5. Delacour, D., Salomon, J., Robine, S., and Louvard, D. (2016). Plasticity of the brush border - the yin and yang of intestinal homeostasis. Nat. Rev. Gastroenterol. Hepatol. *13*, 161–174. https://doi.org/10.1038/nrgastro.2016.5.
6. Charbit-Henrion, F., Parlato, M., Malamut, G., Ruemmele, F., and Cerf-Bensussan, N. (2021). Intestinal immunoregulation: lessons from human mendelian diseases. Mucosal Immunol. *14*, 1017–1037. https://doi.org/10.1038/s41385-021-00398-3.
7. Babcock, S.J., Flores-Marin, D., and Thiagarajah, J.R. (2023). The genetics of monogenic intestinal epithelial disorders. Hum. Genet. *142*, 613–654. https://doi.org/10.1007/s00439-022-02501-5.
8. Muller, T., Hess, M.W., Schiefermeier, N., Pfaller, K., Ebner, H.L., Heinz-Erian, P., Ponstingl, H., Partsch, J., Rollinghoff, B., Kohler, H., et al. (2008). MYO5B mutations cause microvillus inclusion disease and disrupt epithelial cell polarity. Nat. Genet. *40*, 1163–1165. https://doi.org/10.1038/ng.225.
9. Duclaux-Loras, R., Lebreton, C., Berthelet, J., Charbit-Henrion, F., Nicolle, O., Revenu des Courtils, C., Waich, S., Valovka, T., Khiat, A., Rabant, M., et al. (2022). UNC45A deficiency causes microvillus inclusion disease-like phenotype by impairing myosin VB-dependent apical trafficking. J. Clin. Invest. *132*, e154997. https://doi.org/10.1172/jci154997.
10. Li, Q., Zhou, Z., Sun, Y., Sun, C., Klappe, K., and van IJzendoorn, S.C.D. (2022). A Functional Relationship Between UNC45A and MYO5B Connects Two Rare Diseases With Shared Enteropathy. Cell. Mol. Gastroenterol. Hepatol. *14*, 295–310. https://doi.org/10.1016/j.jcmgh.2022.04.006.
11. Esteve, C., Francescatto, L., Tan, P.L., Bourchany, A., De Leusse, C., Marinier, E., Blanchard, A., Bourgeois, P., Brochier-Armanet, C., Bruel, A.L., et al. (2018). Loss-of-Function Mutations in UNC45A Cause a Syndrome Associating Cholestasis, Diarrhea, Impaired Hearing, and Bone Fragility. Am. J. Hum. Genet. *102*, 364–374. https://doi.org/10.1016/j.ajhg.2018.01.009.
12. Almeida, C.G., Yamada, A., Tenza, D., Louvard, D., Raposo, G., and Coudrier, E. (2011). Myosin 1b promotes the formation of post-Golgi carriers by regulating actin assembly and membrane remodelling at the trans-Golgi network. Nat. Cell Biol. *13*, 779–789. https://doi.org/10.1038/ncb2262.
13. Prosperi, M.T., Lepine, P., Dingli, F., Paul-Gilloteaux, P., Martin, R., Loew, D., Knolker, H.J., and Coudrier, E. (2015). Myosin 1b functions as an effector of EphB signaling to control cell repulsion. J. Cell Biol. *210*, 347–361. https://doi.org/10.1083/jcb.201501018.
14. Iuliano, O., Yoshimura, A., Prosperi, M.T., Martin, R., Knolker, H.J., and Coudrier, E. (2018). Myosin 1b promotes axon formation by regulating actin wave propagation and growth cone dynamics. J. Cell Biol. *217*, 2033–2046. https://doi.org/10.1083/jcb.201703205.
15. Yamada, A., Mamane, A., Lee-Tin-Wah, J., Di Cicco, A., Prévost, C., Lévy, D., Joanny, J.F., Coudrier, E., and Bassereau, P. (2014). Catch-bond behaviour facilitates membrane tubulation by non-processive myosin 1b. Nat. Commun. *5*, 3624. https://doi.org/10.1038/ncomms4624.
16. Pernier, J., Morchain, A., Caorsi, V., Bertin, A., Bousquet, H., Bassereau, P., and Coudrier, E. (2020). Myosin 1b flattens and prunes branched actin filaments. J. Cell Sci. *133*, jcs247403. https://doi.org/10.1242/jcs.247403.
17. Pernier, J., Kusters, R., Bousquet, H., Lagny, T., Morchain, A., Joanny, J.F., Bassereau, P., and Coudrier, E. (2019). Myosin 1b is an actin

depolymerase. Nat. Commun. *10*, 5200. https://doi.org/10.1038/s41467-019-13160-y.

18. Gazda, L., Pokrzywa, W., Hellerschmied, D., Löwe, T., Forné, I., Mueller-Planitz, F., Hoppe, T., and Clausen, T. (2013). The myosin chaperone UNC-45 is organized in tandem modules to support myofilament formation in C. elegans. Cell *152*, 183–195. https://doi.org/10.1016/j.cell.2012.12.025.
19. Roland, J.T., Bryant, D.M., Datta, A., Itzen, A., Mostov, K.E., and Goldenring, J.R. (2011). Rab GTPase-Myo5B complexes control membrane recycling and epithelial polarization. Proc. Natl. Acad. Sci. USA *108*, 2789–2794. https://doi.org/10.1073/pnas.1010754108.
20. Boncompain, G., Divoux, S., Gareil, N., de Forges, H., Lescure, A., Latreche, L., Mercanti, V., Jollivet, F., Raposo, G., and Perez, F. (2012). Synchronization of secretory protein traffic in populations of cells. Nat. Methods *9*, 493–498. https://doi.org/10.1038/nmeth.1928.
21. Koreishi, M., Gniadek, T.J., Yu, S., Masuda, J., Honjo, Y., and Satoh, A. (2013). The golgin tether giantin regulates the secretory pathway by controlling stack organization within Golgi apparatus. PLoS One *8*, e59821. https://doi.org/10.1371/journal.pone.0059821.
22. Gillingham, A.K., and Munro, S. (2016). Finding the Golgi: Golgin Coiled-Coil Proteins Show the Way. Trends Cell Biol. *26*, 399–408. https://doi.org/10.1016/j.tcb.2016.02.005.
23. Liu, Y., Xu, X.H., Chen, Q., Wang, T., Deng, C.Y., Song, B.L., Du, J.L., and Luo, Z.G. (2013). Myosin Vb controls biogenesis of post-Golgi Rab10 carriers during axon development. Nat. Commun. *4*, 2005. https://doi.org/10.1038/ncomms3005.
24. Leng, C., Overeem, A.W., Cartón-Garcia, F., Li, Q., Klappe, K., Kuipers, J., Cui, Y., Zuhorn, I.S., Arango, D., and van IJzendoorn, S.C.D. (2019). Loss of MYO5B expression deregulates late endosome size which hinders mitotic spindle orientation. PLoS Biol. *17*, e3000531. https://doi.org/10.1371/journal.pbio.3000531.
25. Wallace, K.N., Akhter, S., Smith, E.M., Lorent, K., and Pack, M. (2005). Intestinal growth and differentiation in zebrafish. Mech. Dev. *122*, 157–173. https://doi.org/10.1016/j.mod.2004.10.009.
26. Crosnier, C., Vargesson, N., Gschmeissner, S., Ariza-McNaughton, L., Morrison, A., and Lewis, J. (2005). Delta-Notch signalling controls commitment to a secretory fate in the zebrafish intestine. Development *132*, 1093–1104. https://doi.org/10.1242/dev.01644.
27. Ng, A.N.Y., de Jong-Curtain, T.A., Mawdsley, D.J., White, S.J., Shin, J., Appel, B., Dong, P.D.S., Stainier, D.Y.R., and Heath, J.K. (2005). Formation of the digestive system in zebrafish: III. Intestinal epithelium morphogenesis. Dev. Biol. *286*, 114–135. https://doi.org/10.1016/j.ydbio.2005.07.013.
28. Hegan, P.S., Mermall, V., Tilney, L.G., and Mooseker, M.S. (2007). Roles for Drosophila melanogaster myosin IB in maintenance of enterocyte brush-border structure and resistance to the bacterial pathogen Pseudomonas entomophila. Mol. Biol. Cell *18*, 4625–4636. https://doi.org/10.1091/mbc.e07-02-0191.
29. Tyska, M.J., Mackey, A.T., Huang, J.D., Copeland, N.G., Jenkins, N.A., and Mooseker, M.S. (2005). Myosin-1a is critical for normal brush border structure and composition. Mol. Biol. Cell *16*, 2443–2457. https://doi.org/10.1091/mbc.E04-12-1116.
30. Sidhaye, J., Pinto, C.S., Dharap, S., Jacob, T., Bhargava, S., and Sonawane, M. (2016). The zebrafish goosepimples/myosin Vb mutant exhibits cellular attributes of human microvillus inclusion disease. Mech. Dev. *142*, 62–74. https://doi.org/10.1016/j.mod.2016.08.001.
31. Alvers, A.L., Ryan, S., Scherz, P.J., Huisken, J., and Bagnat, M. (2014). Single continuous lumen formation in the zebrafish gut is mediated by smoothened-dependent tissue remodeling. Development *141*, 1110–1119. https://doi.org/10.1242/dev.100313.
32. Horne-Badovinac, S., Lin, D., Waldron, S., Schwarz, M., Mbamalu, G., Pawson, T., Jan, Y., Stainier, D.Y., and Abdelilah-Seyfried, S. (2001). Positional cloning of heart and soul reveals multiple roles for PKC lambda in zebrafish organogenesis. Curr. Biol. *11*, 1492–1502. https://doi.org/10.1016/s0960-9822(01)00458-4.
33. Thisse, B., and Thisse, C. (2004). Fast Release Clones: A High Throughput Expression Analysis. ZFIN Direct Data Submission. http://zfin.org.
34. Kok, F.O., Shin, M., Ni, C.W., Gupta, A., Grosse, A.S., van Impel, A., Kirchmaier, B.C., Peterson-Maduro, J., Kourkoulis, G., Male, I., et al. (2015). Reverse genetic screening reveals poor correlation between morpholino-induced and mutant phenotypes in zebrafish. Dev. Cell *32*, 97–108. https://doi.org/10.1016/j.devcel.2014.11.018.
35. Rossi, A., Kontarakis, Z., Gerri, C., Nolte, H., Hölper, S., Krüger, M., and Stainier, D.Y.R. (2015). Genetic compensation induced by deleterious mutations but not gene knockdowns. Nature *524*, 230–233. https://doi.org/10.1038/nature14580.
36. El-Brolosy, M.A., and Stainier, D.Y.R. (2017). Genetic compensation: A phenomenon in search of mechanisms. PLoS Genet. *13*, e1006780. https://doi.org/10.1371/journal.pgen.1006780.
37. Benesh, A.E., Nambiar, R., McConnell, R.E., Mao, S., Tabb, D.L., and Tyska, M.J. (2010). Differential localization and dynamics of class I myosins in the enterocyte microvillus. Mol. Biol. Cell *21*, 970–978. https://doi.org/10.1091/mbc.e09-07-0638.
38. Revenu, C., Ubelmann, F., Hurbain, I., El-Marjou, F., Dingli, F., Loew, D., Delacour, D., Gilet, J., Brot-Laroche, E., Rivero, F., et al. (2012). A new role for the architecture of microvillar actin bundles in apical retention of membrane proteins. Mol. Biol. Cell *23*, 324–336. https://doi.org/10.1091/mbc.E11-09-0765.
39. Mazzolini, R., Dopeso, H., Mateo-Lozano, S., Chang, W., Rodrigues, P., Bazzocco, S., Alazzouzi, H., Landolfi, S., Hernández-Losa, J., Andretta, E., et al. (2012). Brush border myosin Ia has tumor suppressor activity in the intestine. Proc. Natl. Acad. Sci. USA *109*, 1530–1535. https://doi.org/10.1073/pnas.1108411109.
40. Komaba, S., and Coluccio, L.M. (2015). Myosin 1b Regulates Amino Acid Transport by Associating Transporters with the Apical Plasma Membrane of Kidney Cells. PLoS One *10*, e0138012. https://doi.org/10.1371/journal.pone.0138012.
41. Mammoto, T., and Ingber, D.E. (2010). Mechanical control of tissue and organ development. Development *137*, 1407–1420. https://doi.org/10.1242/dev.024166.
42. Reymann, A.C., Boujemaa-Paterski, R., Martiel, J.L., Guérin, C., Cao, W., Chin, H.F., De La Cruz, E.M., Théry, M., and Blanchoin, L. (2012). Actin network architecture can determine myosin motor activity. Science *336*, 1310–1314. https://doi.org/10.1126/science.1221708.
43. Coudrier, E., and Almeida, C.G. (2011). Myosin 1 controls membrane shape by coupling F-Actin to membrane. BioArchitecture *1*, 230–235. https://doi.org/10.4161/bioa.18406.
44. Salas-Cortes, L., Ye, F., Tenza, D., Wilhelm, C., Theos, A., Louvard, D., Raposo, G., and Coudrier, E. (2005). Myosin Ib modulates the morphology and the protein transport within multi-vesicular sorting endosomes. J. Cell Sci. *118*, 4823–4832. https://doi.org/10.1242/jcs.02607.
45. Buske, P., Przybilla, J., Loeffler, M., Sachs, N., Sato, T., Clevers, H., and Galle, J. (2012). On the biomechanics of stem cell niche formation in the gut–modelling growing organoids. FEBS J. *279*, 3475–3487. https://doi.org/10.1111/j.1742-4658.2012.08646.x.
46. Dudouet, B., Robine, S., Huet, C., Sahuquillo-Merino, C., Blair, L., Coudrier, E., and Louvard, D. (1987). Changes in villin synthesis and subcellular distribution during intestinal differentiation of HT29-18 clones. J. Cell Biol. *105*, 359–369.
47. Dereeper, A., Guignon, V., Blanc, G., Audic, S., Buffet, S., Chevenet, F., Dufayard, J.F., Guindon, S., Lefort, V., Lescot, M., et al. (2008). Phylogeny.fr: robust phylogenetic analysis for the non-specialist. Nucleic Acids Res. *36*, W465–W469. https://doi.org/10.1093/nar/gkn180.
48. Kwan, K.M., Fujimoto, E., Grabher, C., Mangum, B.D., Hardy, M.E., Campbell, D.S., Parant, J.M., Yost, H.J., Kanki, J.P., and Chien, C.B. (2007). The Tol2kit: a multisite gateway-based construction kit for Tol2 transposon

transgenesis constructs. Dev. Dyn. *236*, 3088–3099. https://doi.org/10.1002/dvdy.21343.

49. Dalgin, G., Ward, A.B., Hao, L.T., Beattie, C.E., Nechiporuk, A., and Prince, V.E. (2011). Zebrafish mnx1 controls cell fate choice in the developing endocrine pancreas. Development *138*, 4597–4608. https://doi.org/10.1242/dev.067736.
50. Distel, M., Wullimann, M.F., and Köster, R.W. (2009). Optimized Gal4 genetics for permanent gene expression mapping in zebrafish. Proc. Natl. Acad. Sci. USA *106*, 13365–13370. https://doi.org/10.1073/pnas.0903060106.
51. Horstick, E.J., Jordan, D.C., Bergeron, S.A., Tabor, K.M., Serpe, M., Feldman, B., and Burgess, H.A. (2015). Increased functional protein expression using nucleotide sequence features enriched in highly expressed genes in zebrafish. Nucleic Acids Res. *43*, e48. https://doi.org/10.1093/nar/gkv035.
52. Albadri, S., Del Bene, F., and Revenu, C. (2017). Genome editing using CRISPR/Cas9-based knock-in approaches in zebrafish. Methods *121–122*, 77–85. https://doi.org/10.1016/j.ymeth.2017.03.005.
53. Robine, S., Huet, C., Moll, R., Sahuquillo-Merino, C., Coudrier, E., Zweibaum, A., and Louvard, D. (1985). Can villin be used to identify malignant and undifferentiated normal digestive epithelial cells? Proc. Natl. Acad. Sci. USA *82*, 8488–8492. https://doi.org/10.1073/pnas.82.24.8488.
54. Kolotuev, I., Bumbarger, D.J., Labouesse, M., and Schwab, Y. (2012). Targeted ultramicrotomy: a valuable tool for correlated light and electron microscopy of small model organisms. Methods Cell Biol. *111*, 203–222. https://doi.org/10.1016/B978-0-12-416026-2.00011-X.

STAR★METHODS

KEY RESOURCES TABLE

REAGENT or RESOURCE	SOURCE	IDENTIFIER
Antibodies		
Rabbit MYO1B	Recombinant antibody facility of Institut Curie, Paris, France	Salas-Cortes et al.[44]
Rabbit GAPDH (14C10)	Cell Signaling	Cat#2118; RRID:AB_1642205
Rabbit HSP90	Cell Signaling	Cat#4874; RRID:AB_2121214
Rabbit β−tubulin (9F3)	Cell Signaling	Cat#2128; RRID:AB_823664
Mouse Villin (ID2C3)	Sylvie ROBINE, UMR144, Institut Curie, Paris, France	Dudouet et al.[46]
Rabbit pERM	Abcam	Cat#ab47293; RRID:AB_873790
Mouse Lamp1 (H4A3)	Abcam	Cat#ab25630; RRID:AB_470708
Rabbit Giantin (TA10)	Recombinant antibody facility of Institut Curie, Paris, France	Recombinant Antibody Platform TAb-IP A-R-R#05
Mouse Golgin97 (CDF4)	Thermo Fisher	Cat#A-21270; RRID:AB_221447
Mouse 2F11	Abcam	Cat#ab71286; RRID:AB_1209226
Mouse Cytokeratin (AE1/AE3)	Biorad	Cat#MCA1907; RRID:AB_2134031
Rabbit Myo1b	Novus Biologicals	Cat# NBP1-87739
Mouse FLAG (M2)	Sigma-Aldrich	Cat#F3165; RRID:AB_259529
Anti-rabbit IgG, HRP-linked	Cell Signaling	Cat#7074 RRID:AB_2099233
Goat anti-rabbit-Alexa Fluor 635	Molecular probes	Cat# **A-31576** RRID: AB_2536186
Goat anti-rabbit-Alexa Fluor 488	Molecular probes	Cat# A32731 RRID: AB_2633280
Alexa Fluor 488 AffiniPure Donkey Anti-Mouse IgG (H + L)	Jackson ImmunoResearch	715-545-151 RRID:AB_2341099
Cy3 AffiniPure Donkey Anti-Rabbit IgG (H + L)	Jackson ImmunoResearch	711-165-152 RRID:AB_2307443
Biological samples		
Intestinal tissue from UNC45A deficient patient (c.710 T>C; p.Leu237Pro) (gender: F)	Pathology Department Necker-Enfants Malades Hospital, Paris, FR	Duclaux-Loras et al.[9]
Intestinal tissue from control individual (gender: F)	Pathology Department Necker-Enfants Malades Hospital, Paris, FR	Duclaux-Loras et al.[9]
Chemicals, peptides, and recombinant proteins		
proteasome inhibitor MG132	Sigma-Aldrich	Cat#M7449
Matrigel	Corning	Cat#354230
Puromycin	Sigma-Aldrich	Cat#P4512
Biotin	Sigma-Aldrich	Cat#B4501
RIPA buffer	Millipore	Cat#20-188
Protease Inhibitor Cocktail	Roche	Cat#11836170001
Antigen Unmasking Solution	Vector Laboratories	Cat#H-3300-250
Phalloidin-Alexa Fluor 488	Invitrogen	Cat#A12379
Phalloidin-Alexa Fluor 568	Invitrogen	Cat#A12380
Hoechst 33342	ENZO	Cat#639
Paraformaldehyde	Electron Microscopy Sciences	Cat#EM-15710,

(*Continued on next page*)

Continued

REAGENT or RESOURCE	SOURCE	IDENTIFIER
DAPI	Sigma-Aldrich	Cat#D9542
MS-222 (Ethyl-3-aminobenzoate de methanesulfonate)	Sigma-Aldrich	Cat#E10521
PTU (1-phenyl 2-thiourea)	Sigma-Aldrich	Cat#P7629
Cas9	NEB	Cat# M0386
TRIzol	Invitrogen	Cat#15596026
Mowiol 4-88	Merck Millipore, Calbiochem	Cat#475904
Saponin	Merck Millipore, Calbiochem	Cat#15137845
Leibovitz's L-15 medium	Gibco, Thermo Fisher Scientific	Cat#21083027
Critical commercial assays		
Click-iT EdU Imaging Kit	Invitrogen	Cat# C10337
Proteostat Aggresome Detection Kit	ENZO	Cat#ENZ-51035
μMACS c-myc Isolation Kit	Miltenyi Biotec	Cat#130-091-123
Gibson Assembly Cloning Kit	New England Biolabs	Cat#E5510S
DIG RNA labeling Kit	Roche	Cat#11 175 025 910
ApopTag Red *In situ* Apoptosis detection kit	Sigma-Aldrich	Cat#S7165
Multisite Gateaway	Invitrogen	Cat#2537-023
Megascript T7 transcription kit	Ambion	Cat#AM1334
RNAeasy Mini Kit	Quiagen	Cat#74104
SuperScript III First-Strand Synthesis System	Invitrogen	Cat#10246902
TURBO DNA-free kit	ThermoFisher Scientific	Cat#10792877
SYBR Green PCR Master Mix	ThermoFisher Scientific	Cat#4344463
TransIT®-Lenti Transfection reagent	Mirus	Cat#MIR6604
Experimental models: Cell lines		
HEK293T cells	Takara	Cat#632180
Caco-2 cells	ATCC	Cat#HTB37
NT-Caco-2 cells	N/A	Duclaux-Loras et al.[9]
MYO1B KO-Caco-2 cells	N/A	Duclaux-Loras et al.[9]
MYO5B KO -Caco-2 cells	This study	N/A
UNC45A-FLAG-MYC- Caco-2 cells	N/A	Duclaux-Loras et al.[9]
NT-Caco-2-GPI cells	This study	N/A
MYO1B KO-Caco-2-GPI cells	This study	N/A
MYO5B KO -Caco-2-GPI cells	This study	N/A
NT-Caco-2-ALPI cells	This study	N/A
MYO1B KO-Caco-2-ALPI cells	This study	N/A
MYO5B KO -Caco-2-ALPI cells	This study	N/A
Experimental models: Organisms/strains		
cldn15la:cldn15la-GFP	M. Bagnat, Department of Cell Biology, Duke University Medical Center, Durham, NC 27710, USA	Alvers et al.[31]
Tupfel Long-Fin (TL) Wildtype Zebrafish	EZRC (https://www.ezrc.kit.edu/)	ZDB-GENO-990623-2
βactinhsp70:KalT4; cmlc2:eGFP Zebrafish	This study	N/A
14UAS:ubc-eGFP-Myo1b Zebrafish	This study	N/A
Oligonucleotides		
sgRNA h-MYO1B, for 5-CACCGAT CCCTACGAGATCAAGATA-3	Thermo Fisher Scientific	N/A
sgRNA h-MYO1B, rev 5-AAACTAT CTTGATCTCGTAGGGATC-3	Thermo Fisher Scientific	N/A

(*Continued on next page*)

Continued

REAGENT or RESOURCE	SOURCE	IDENTIFIER
sgRNA h-MYO5B, for 5- GACCAT CAGTCCATCATAGTCAGTGGGG-3	Thermo Fisher Scientific	N/A
sgRNA h-MYO5B, rev-5-CCCCA CTGACTATGATGGACTGATGGTC-3	Thermo Fisher Scientific	N/A
sgRNA NT, for 5-CAACCGGACAA TCATGGTGAAAGCGG-3	Thermo Fisher Scientific	N/A
sgRNA NT, rev 5- AAACCCGCTTT CACCATGATTGTCC-5′	Thermo Fisher Scientific	N/A
sgB: 5-CTTCTGACAAGGGCTCTAGG-3	Integrated DNA Technologies	N/A
Myo1b-MO, 5-ATGAGAAACTGT GTTCATTACCTGG-3	Gene Tools	N/A
control-MO, 5-CCTCCTACCTCAG TTACAATTTATA-3	Gene Tools	N/A
myo1b sense: 5-CAA TAT GAT AGG GGT AGG GGA CAT G;	Eurofins	N/A
myo1b antisense: 5- TGG TTT GAA CTC AAT ATT TCC CAG C	Eurofins	N/A
Recombinant DNA		
lentiCRISPRv2	Addgene	#98290
UNC45A-FLAG-MYC overexpression vector	pLVX-EF1α-IRES-mCherry vector	Duclaux-Loras et al.[9]
pCDH1_Str-KDEL_SBP-EGFP-GPI	Addgene	#65294
pCDH1_Str-KDEL_SBP-EGFP-ALPI	This study	N/A
psPAX2	Addgene	#12260
pMD2.G	Addgene	#12259
pβactinhsp70:KalT4; cmlc2:eGFP	This study	N/A
p*14UAS:ubc-eGFP-Myo1b*	This study	N/A
pT1UciMP	Addgene	#62215
pCR-bluntII-TOPO	Invitrogen	10434012
pDR274	Addgene	#42250
Software and algorithms		
MetaMorph software	Molecular Devices	http://www.moleculardevices.com/Products/Software/Meta-Imaging-Series/MetaMorph.html RRID:SCR_002368
Imaris software	Oxford Instruments	http://www.bitplane.com/imaris/imaris RRID:SCR_007370
ImageJ-Fiji	Image Software	https://imagej.net/RRID:SCR_003070
Huygens Professional Software	Scientific Volume Imaging (SVI)	https://svi.nl/Huygens-Professional
GraphPad Prism v10	Graphpad Prism Inc	http://www.graphpad.com/RRID:SCR_002798
Other		
μ-Slide 8 Well	iBIDI	Cat#80821
Tissue-Tek O.C.T. Compound	Sakura	Cat#4583
Epoxy resin mix: Araldite M, Epon 812,Hardener DDSA, DMP-30	Sigma-Aldrich	Cat#10951; Cat#45345; Cat#45346; Cat#93331
Adhesive Frames GENE-FRAME 65 μL	Thermo Fisher Scientific	Cat#AB0577
Formvar-coated slot grids	Electron Microscopy Sciences	Cat#FCF2010-CU
Mini-PROTEAN® TGX™ Stain Free Precast Gels	Biorad	Cat#456-8084

EXPERIMENTAL MODEL AND STUDY PARTICIPANT DETAILS

Zebrafish (*Danio rerio*) husbandry

Wild-type Tupfel long fin zebrafish strains were used and raised according to standard protocols. Stable transgenic lines were generated by injection of the plasmids with *tol2* or *tol1 transposase* mRNA at 25 ng/μL in one-cell stage zebrafish embryos. The transgenic BAC line claudin15-like-a fused to GFP (*cldn15la*:cldn15la-GFP) was kindly provided by Michel Bagnat.[31] For live-imaging, larvae were anesthetized in 0.02% MS-222 (Sigma-Aldrich) and immobilized in 1% low melting point agarose. Imaging was performed on a Zeiss LSM 780 confocal.

Caco-2 culture and cyst generation

Caco-2 cells were cultured in DMEM (Gibco) with 10% FCS containing 4% Matrigel (BD Biosciences) To detect aggregation-prone proteins, the proteasome inhibitor MG132 (Sigma-Aldrich) was added overnight in the culture medium at a concentration of 10 μM. To generate cysts, Caco-2 cells were resuspended at a concentration of 10^4 cells/mL in DMEM (Gibco) with 20% FCS containing 4% Matrigel (BD Biosciences) and 250 μL were plated in 8-wells chamber slide IBIDI (Biovalley), previously precoated with 100 μL of Matrigel and grown for 5 days.

Experimental animal study approval

All animal procedures were performed in accordance with the animal welfare guidelines of France and the European Union. Animal experimentations were approved by the committee on ethics of animal experimentation at Institut Curie and Institut de la Vision, Paris (APAFIS#21323–2019062416186982).

METHOD DETAILS

CRISPR/Cas9 genome editing of *MYO1B* and *MYO5B* in Caco-2 cells

The single-guide RNAs (sgRNAs) were designed using the CRISPR Design Tool (Massachusetts Institute of Technology) and cloned into the BsmbI site of the lentiCRISPRv2 plasmid (#98290, Addgene). sgRNA targeting MYO1B: for-5- CACCGATCCCTAC GAGATCAAGATA -3, rev-5- AAAC TA TCT TGA TCT CGT AGG GAT C −3 and sgRNA targeting MYO5B: for-5- GACCATCAGT CCATCATAGTCAGTGGGG-3, rev-5-CCCCACTGACTATGATGGACTGATGGTC-3. Caco-2 cells (NT, MYO1B KO and MYO5B KO) were obtained by transduction with lentiviral particles produced in HEK293T cells (Takara) using pMD.2g (Addgene) as envelope and pPAX2 (Addgene) as packaging. A clonal population was then selected using puromycin resistance (10 μg/mL) and limiting dilution.

Real-time imaging of the synchronized secretion

Caco-2 cells (NT, MYO1B KO and MYO5B KO) stably expressing Str-KDEL as a hook and either SBP-EGFP-ALPI or SBP-EGFP-GPI as a reporter were obtained by transduction with lentiviral particles produced in HEK293T cells (Takara) using pMD.2g (Addgene) as envelope and pPAX2 (Addgene) as packaging. For Imaging, Caco-2 cells expressing RUSH constructs were grown on 25-mm glass coverslips, which were then transferred to an L-shape tubing-equipped Chamlide chamber (Live Cell Instrument). Trafficking was induced by exchanging Leibovitz medium (Life Technologies) with prewarmed Leibovitz medium supplemented with 40 μM biotin (B4501; Sigma-Aldrich). Imaging was performed at 37°C in a thermostat-controlled chamber using an Eclipse 80i microscope (Nikon) equipped with a spinning disc confocal head (Perkin) and an Ultra897 iXon camera (Andor). Image acquisition was performed using MetaMorph software (Molecular Devices).

Western blotting and pull down assay

Caco-2 cells were lysed in RIPA buffer (Sigma-Aldrich) supplemented with complete protease inhibitor (Roche, Sigma Aldrich). 20 μg of extracts in Laemmli buffer were loaded on a 4–15% polyacrylamide gradient concentration gel (Biorad). Adult zebrafish guts were dissected on ice and mechanically lysed in 200μL lysis buffer (10 mM HEPES +300 mM KCl +5 mM MgCl2 + 0.45% Triton X100 + 0.05% Tween 20, pH7) with 10 mM ATP and Complete protease inhibitor (Roche, Sigma Aldrich). 40 μg of extracts in Laemmli buffer were loaded on a 4–12% polyacrylamide gradient concentration gel (ThermoFisher). Primary antibodies used were rabbit anti-rat Myo1b (1.8 μg/μL, 1:500[44]), anti GAPDH (#14C10, 1:1000, Cell Signaling), anti HSP90 (#4874, 1:1000, Cell Signaling), anti-FLAG (#F3165, 1:1000, Sigma-Aldrich). For immunoprecipitation, myc-tagged UNC45A Caco-2 cells and myc-tagged empty vector (EV) control Caco-2 cells were lysed in buffer (10 mM Tris/HCl, 150 mM NaCl, 0.5 mM EDTA, 0.5% NP40) with complete protease inhibitors (Roche, Sigma-Aldrich), and myc-tagged proteins were immunoprecipitated by using the μMACS c-myc Isolation Kit (Miltenyi Biotec) according to the manufacturer's instructions.

Phylogenetic analysis

The Myo1b and Myo1a homologs in Danio rerio, Homo sapiens, Mus Musculus, Gallus gallus and Drosophila melanogaster were obtained from NCBI HomoloGene. Protein sequences were aligned and a phylogenetic tree was assembled using the online 'One Click' mode at Phylogeny.fr.[47]

Molecular cloning

The *βactinhsp70:KalT4;cmlc2:eGFP* construct was generated by combining four plasmids using the Multisite Gateway system (Invitrogen): p5E-bactinhsp70, pME-KalT4, p3E-polyA and pDEST-*cmcl2*:eGFP containing Tol2 sites.[48] The βactin promoter was cloned into the pCR-bluntII-TOPO vector (Invitrogen) and then inserted in the p5E-MCS using KpnI and XhoI restriction sites. The 3′ 638bp of the zebrafish hsp70 promoter[49] was inserted into this p5E-βactin vector linearized with XhoI using the Gibson Assembly Cloning Kit (New England Biolabs). The optimized Gal4 KalT4[50] was amplified and inserted in a pDONR221 using the Multisite Gateway system (Invitrogen). To generate the *14UAS:ubc-eGFP-Myo1b vector*, eGFP-Rat Myo1b cDNA was amplified from a previously published plasmid.[13] It was inserted into the pT1UciMP plasmid containing 14xUAS-ubc and Tol1 sites[51] linearized with Xho1 using the Gibson Assembly Cloning Kit (New England Biolabs).

Zebrafish (*Danio rerio*) husbandry

Wild-type Tupfel long fin zebrafish strains were used and raised according to standard protocols. Stable transgenic lines were generated by injection of the plasmids with *tol2* or *tol1 transposase* mRNA at 25 ng/μL in one-cell stage zebrafish embryos. The transgenic BAC line claudin15-like-a fused to GFP (*cldn15la*:cldn15la-GFP) was kindly provided by Michel Bagnat.[31] For live-imaging, larvae were anesthetized in 0.02% MS-222 (Sigma-Aldrich) and immobilized in 1% low melting point agarose. Imaging was performed on a Zeiss LSM 780 confocal. All animal procedures were performed in accordance with French and European Union animal welfare guidelines.

In situ hybridization

In situ hybridizations (ISH) were performed on larvae treated with 1-phenyl-2-thiourea (PTU, Sigma-Aldrich) and fixed in freshly made 4% paraformaldehyde (PFA) 2-4h at RT and stored in 100% methanol at −20°C. After rehydration, larvae were treated with proteinase K (20 μg/mL; Roche diagnostics) at RT for 1h (3dpf) or 2h (5dpf) and fixed again in 4% PFA at RT for 20min. Digoxigenin-labeled antisense and sense RNA probes were synthesized by *in vitro* transcription using DIG-labeled UTP according to the manufacturer's instructions (DIG RNA labeling kit, Roche). Primers used were as follow: *myo1b* sense: CAA TAT GAT AGG GGT AGG GGA CAT G; antisense: TGG TTT GAA CTC AAT ATT TCC CAG C. Anti-DIG antibody conjugated to alkaline phosphatase allowed detection of hybridized riboprobes according to the manufacturer's instructions (Roche).

Myo1b zebrafish mutant generation with CRISPR/Cas9

The sgRNA sequence (sgB: 5′CTTCTGACAAGGGCTCTAGG) was cloned into the BsaI digested pDR274 vector (Addgene). The sgRNAs were synthesized by *in vitro* transcription (Megascript T7 transcription kit, Ambion). After transcription, sgRNAs were purified using the RNAeasy Mini Kit (Quiagen). For injections at one cell stage, the synthesized sgB was injected at 300 ng/μL after 5-min incubation at RT with Cas9 protein (NEB) at 2μM final in 20mM Hepes-NaOH pH 7.5, 150mM KCl.[52] Injected embryos were grown to adulthood and crossed with wild-types to identify founders. Pools of 20 embryos per clutch were lysed in NaOH 50 mM at 95°C for at least 30min. PCR was performed on lysates to amplify the genomic region targeted by the sgB with primers forward 5′GGGTGTTGTTCAGCGATGGA and reverse 5′ATAGATCTCATTGTGATCGA using Phusion High-Fidelity DNA polymerase (Thermo Scientific). The amplicons were cloned in pCR-bluntII-TOPO vector (Zero Blunt Topo PCR cloning kit, Invitrogen) and sequenced (GATC Biotech) to identify indels and the corresponding founder fish. Sequences were analyzed using Geneious. After selection of the founder, genotyping of the line was performed by PCR on fin clips with primers 5′AGATGAATGCAAGCAAGCCATT and 5′ATACGATCTGATTGTGATCGAATCGCT. The resulting product was digested with restriction enzyme FspBI, the site of which is lost in the mutant, resulting in 2 fragments (208 and 66bp) for the WT allele and only one (275bp) for the mutated allele.

Morpholino oligonucleotide design and injections

Myo1b splice blocking Morpholino was designed to target the splice donor site downstream of exon 22 (Myo1b-MO, 5′-ATGA GAAACTGTGTTCATTACCTGG). Experiments were performed in parallel with a standard control-MO (5′-CCTCCTACCTCAGTTA CAATTTATA) with no target in the zebrafish genome. Morpholinos (Gene Tools) diluted at 1mM in water, were injected in 1-cell stage embryos at a final concentration of 0.2mM. To validate Myo1b-MO knock-down, RT-PCR was performed on 3dpf larvae. Total RNA of 50 larvae was prepared with TRIzol and TURBO DNAse-free reagents (Invitrogen). mRNA (1μg) was retro-transcribed using oligo(dT) primers and the SuperScript III First-Strand Synthesis System (Invitrogen). To amplify the region targeted by the MO (Figure S1A), PCR was performed on the cDNA with two different forward primers (primer 1 in exon21 was: 5′GGCTGCGATATTCT TGCCTCC, primer 2 at the edge of exon22 and the targeted intron was: 5′TCTTTCATTCGTGGATGGAAGGCC) and the reverse primer 5′AACCCAGGTAATGAACACAGTTTCTAT. PCR products were run on a gel (Figure S3B) and bands were gel purified (Macherey-Nagel), inserted in a pCR-bluntII-Topo vector (Invitrogen) and sent for sequencing (GATC) to assess intron retention.

Quantitative RT-PCR

For each experiment, total RNA was prepared from 3 pools of 50 embryos per phenotype with TRIzol (Invitrogen) reagent and the TURBO DNA-free kit (ThermoFisher Scientific). RNA (1μg) was retro-transcribed using random primers and the SuperScript III First-Strand Synthesis system (ThermoFisher Scientific). For RT-QPCR, the SYBR Green PCR Master Mix (ThermoFisher Scientific) was used according to the manufacturer's instructions and PCR were performed on an ABI PRISM 7900HT instrument. Experimental

triplicates of each sample were averaged and the relative expression level quantified with the log2ΔCT method using EF1a gene. Shown are values normalized on the wild-type samples.

Imaging

Caco-2 cells and cysts were fixed in 4% PFA 30 min at 37°C and washed with PBS. They were permeabilized in PBS, 0.2%TX100, 1% BSA for 5 min at RT and blocked in PBS 3% BSA for 1–2 h at RT. Primary antibodies used were rabbit anti-ratMyo1b (1.8 μg/μL, 1:100[44]), mouse anti-Villin clone ID2C3 (1:300),[53] rabbit anti-pERM (1:100, abcam, #ab47293), mouse anti-Lamp1 clone H4A3 (1:200, abcam, #ab25630), rabbit anti- β−tubulin clone 9F3 (1:200, Cell Signaling, #2128). After washes, they were incubated with Alexa Fluor 488 secondary antibody (Molecular probes, # A32731), phalloidin-Alexa Fluor 568 (ThermoFisher Scientific) and DAPI (Sigma-Aldrich). The Proteostat Aggresome Detection Kit (ENZO, ENZ-51035) was used to assess protein aggregation. Briefly, after the primary antibody rabbit anti-ratMyo1b, cells were incubated for 30 min at RT with goat anti-rabbit-Alexa Fluor 635 antibody (1:400, Molecular probes), Proteostat 1:400 and Hoechst 1:800 (ENZO) in PBS 3%BSA. Myosin1b intensity was quantified on maximal projections of confocal z-stacks of confluent cell monolayers by calculating the sum of all pixel values (raw integrated density, ImageJ). To quantify the colocalization between Myo1b and aggresomes, single confocal planes were thresholded, made binary and ROI were drawn on aggresomes from single cells. The proportions of pixels that are overlapping between the myosin1b and aggresome channels in the ROI were quantified using Manders overlap coefficient with the plugin Intensity Correlation Analysis (ImageJ).

STED imaging was performed using a LEICA SP8 gSTED 2D microscope with an objective HC PL APO CS2 100X/1.4 oil immersion and white light laser with the following acquisition parameters: excitation, 558 nm; depletion, 660 nm, hybrid detector with gating. To improve the signal-to-noise ratio, the images were deconvolved with Huygens Professional Software (Scientific Volume Imaging) using the fast deconvolution presetting. The percentage of area covered by microvilli/cell was measured with ImageJ. The β-angle in the mitotic spindle of Caco-2 cells was calculated with the ImageJ tools x-z confocal sections.[24]

For the analysis of the Golgi morphology in Caco-2 cells, cells were fixed with 3% paraformaldehyde in PBS for 14 min at room temperature. Cells were made permeable with Saponin 1x in PBS 15 min at room temperature and labeled with the appropriate primary antibodies overnight at 4°C in PBS-supplemented Saponin 1x. After washing, cells were incubated 1 h at room temperature with secondary antibodies and DAPI (0.5 μg/mL) in PBS. Coverslips were mounted in Mowiol. Single confocal images were acquired at 63x magnification on an Inverted Leica TCS SP8 MP (Carl Zeiss). Primary antibodies used for the analysis of the Golgi morphology were: rabbit anti-giantin (1:500, clone TA10, recombinant antibody facility of Institut Curie, Paris, France) and mouse anti golgin97 (1:200, Thermo Fisher, A-21270). Secondary antibodies, Alexa Fluor 488 AffiniPure Donkey Anti-Mouse IgG (H + L) (1:400, #715-545-151) and Cy3 AffiniPure Donkey Anti-Rabbit IgG (H + L) (1:400, #711-165-152), were purchased from Jackson ImmunoResearch. Single confocal images were acquired at 63x magnification on an Inverted Leica TCS SP8 MP (Carl Zeiss). Confocal images were first deconvolved using Fiji software to sharpen the distinction between Golgi apparatus and general cytoplasmic fluorescence, and then segmented between Golgi fragments and general cytoplasm on the basis of the intensity of giantin fluorescence using Imaris software. Number of Golgi fragments was determined based on segmentation using Imaris software. Approximately 30 cells were analyzed for each data point.

Zebrafish larvae were fixed for 2h at room temperature in 4% PFA and incubated in 30% sucrose/0.1% PBST overnight at 4°C. They were then frozen in Tissue-Tek OCT (Sakura) at −80°C and sectioned using a Cryostat (Leica). Zebrafish larvae sections were incubated in blocking buffer (10% serum in PBST, PBS 0.1%Tween 20) and with mouse anti-Villin clone ID2C3 (1:300), mouse 2F11 antibody (1:100, Abcam ab71286), cytokeratin pan antibody AE1/AE3 cocktail (1:200, Bio Rad, MCA1907) overnight at 4°C. After washes with PBST, they were incubated with Alexa Fluor 488 secondary antibody (Molecular probes), phalloidin-Alexa Fluor 568 and DAPI. To assess apoptosis, TUNEL assay was performed with reaction solutions from ApopTag Red *In situ* Apoptosis detection kit (Millipore) according to the manufacturer recommendations. To assess proliferation, larvae were injected in the yolk with 10mM 5-ethynyl-2′-deoxyuridine (EDU) in 1% DMSO and incubated in 100μM EdU, 0.4%DMSO for 20 h after injection. Animals were fixed at indicated time and processed according to the Click-iT EdU Imaging Kit (Invitrogen). The numbers of cells were counted manually. only samples displaying single cell layers throughout the entire gut cross-sections were analyzed. The sample size (n =) is defined as the number of larvae analyzed (one section per larva).

Paraffin embedded sections of intestinal tissues from a UNC45A deficient patient (c.710 T>C; p.Leu237Pro) 9 and biopsies from controls were obtained for diagnosis or therapeutic purposes. Duodenal biopsies were routinely fixed in 4% buffered formalin for 24 h and paraffin-embedded. Sections were heated for 1 h at 65°C and paraffin was removed by two 5-min washes in xylene. Sections were then hydrated with ethanol solutions of decreasing concentrations. Unmasking of the epitopes was performed at 100°C for 20 min in Citrate-based Antigen Unmasking Solution (Vector Laboratories). Sections were incubated for 30 min at room temperature in blocking buffer (3% BSA in PBS) and then overnight at 4°C with anti Myo1b antibody (1:200, Novus Biologicals NBP1-87739) in blocking. After washes with PBST, sections were incubated with goat anti rabbit Alexa Fluor 488 antibody (Molecular probes), phalloidin-Alexa Fluor 568 and DAPI for 2 hrs at RT. After extensive washes and mounting in Vectashield (Vector Lab), all stainings were imaged on a LSM780 confocal microscope (Zeiss). Images were processed and numbers of cells quantified using ImageJ.

TEM analysis on zebrafish larvae

5dpf larvae were collected and stored at 4°C in Trump's fixative. Enhanced chemical fixation was performed in a mix of 4% PFA with 2.5% glutaraldehyde in 0.1 mol/L cacodylate buffer overnight at 4°C. A 1.5-h incubation in 1% OsO4 was followed by a 1.5-h incubation with 2% uranyl acetate at ambient temperature. Larvae were then dehydrated through graded ethanol solutions, cleared in acetone, infiltrated, and embedded in Epon-Araldite mix (Araldite M (Sigma 10951), epon 812 (Sigma 45345), Hardener DDSA (Sigma 45346), DMP-30 (Sigma 93331)). We used adhesive frames (GENE-FRAME 65 μL; Thermo Fisher Scientific, AB0577) for flat-embedding, as previously described,[54] to gain better anteroposterior orientation and sectioning. Ultrathin sections were cut on an ultramicrotome (UC7; Leica Microsystems) and collected on formvar-coated slot grids (FCF2010-CU, EMS). Each larva was sectioned transversally in five different places in intestinal bulb with $\geq$20 μm between each grid to examine the sample over a large region. Each grid contained at least 4–6 consecutive sections of 70 nm. TEM grids were observed using a JEM-1400 transmission electron microscope (JEOL) operated at 120 kV, equipped with a Gatan Orius SC1000 camera (Gatan) and piloted by the Digital Micrograph program. Microvilli length and density were quantified using Fiji on TEM pictures of at least 50 MV from 25 enterocytes of 3 larvae per condition.

QUANTIFICATION AND STATISTICAL ANALYSIS

Data were analyzed using GraphPad Prism V10 software (GraphPad Inc). The number of independent biological samples (n) in each experiment is detailed in the figure legends. We applied the non-parametric Mann-Whitney test unless differently indicated in the figure legends. Data are represented as median ±SEM unless differently indicated in the figure legends.